

# Classification and analysis of emission-line galaxies using mean field independent component analysis

James T. Allen,<sup>1,2\*</sup> Paul C. Hewett,<sup>1</sup> Chris T. Richardson,<sup>3</sup> Gary J. Ferland<sup>4</sup> and Jack A. Baldwin<sup>3</sup>

<sup>1</sup>*Institute of Astronomy, University of Cambridge, Madingley Road, Cambridge CB3 0HA*

<sup>2</sup>*Sydney Institute for Astronomy, University of Sydney, 44–70 Rosehill St, Redfern, NSW 2016, Australia*

<sup>3</sup>*Physics & Astronomy Department, Michigan State University, East Lansing, MI 48824-1116, USA*

<sup>4</sup>*Physics & Astronomy Department, University of Kentucky, Lexington, KY 40506-0055, USA*

28 January 2013

## ABSTRACT

We present an analysis of the optical spectra of narrow emission-line galaxies, based on mean field independent component analysis (MFICA), a blind source separation technique. Samples of galaxies were drawn from the Sloan Digital Sky Survey (SDSS) and used to generate compact sets of ‘continuum’ and ‘emission-line’ component spectra. These components can be linearly combined to reconstruct the observed spectra of a wider sample of galaxies. Only 10 components – five continuum and five emission line – are required to produce accurate reconstructions of essentially all narrow emission-line galaxies to a very high degree of accuracy; the median absolute deviations of the reconstructed emission-line fluxes, given the signal-to-noise ratio (S/N) of the observed spectra, are  $1.2\text{--}1.8\sigma$  for the strong lines. After applying the MFICA components to a large sample of SDSS galaxies we identify the regions of parameter space that correspond to pure star formation and pure active galactic nucleus (AGN) emission-line spectra, and produce high S/N reconstructions of these spectra.

The physical properties of the pure star formation and pure AGN spectra are investigated by means of a series of photoionization models, exploiting the faint emission lines that can be measured in the reconstructions. We are able to recreate the emission line strengths of the most extreme AGN case by assuming the central engine illuminates a large number of individual clouds with radial distance and density distributions,  $f(r) \propto r^\gamma$  and  $g(n) \propto n^\beta$ , respectively. The best fit is obtained with  $\gamma = -0.75$  and  $\beta = -1.4$ . From the reconstructed star formation spectra we are able to estimate the starburst ages. These preliminary investigations serve to demonstrate the success of the MFICA-based technique in identifying distinct emission sources, and its potential as a tool for the detailed analysis of the physical properties of galaxies in large-scale surveys.

**Key words:** methods: data analysis – galaxies: active – galaxies: evolution – galaxies: nuclei – galaxies: star formation – galaxies: statistics

## 1 INTRODUCTION

The optical and ultraviolet emission-line spectra of galaxies have proven to be a valuable source of information regarding the physical conditions that prevail within such objects. However, the majority of diagnostics and analysis techniques currently in use focus on measurements of a few small regions of each spectrum, discarding the remaining information. With the greatly increased quality and quantity of data made available by recent extragalactic surveys, new analysis

techniques that make use of all available data are required in order to obtain a more detailed picture of the physical properties and evolution of galaxies.

The classification and analysis of active galactic nuclei (AGN) and star formation (SF) in narrow emission-line galaxies is one area in which updated analysis techniques have the potential to provide new insights into the physical processes that govern these objects. The well-established correlations between the properties of supermassive black holes (SMBHs) and those of their host galaxies (e.g. Magorrian et al. 1998; Ferrarese & Merritt 2000; Kormendy & Gebhardt 2001; Häring & Rix 2004) suggest a strong evolu-

\* E-mail: j.allen@physics.usyd.edu.au

tional link between the two. Feedback processes, in which galaxy-scale winds propelled by the AGN heat and expel the interstellar medium, shutting down both star formation and further black hole accretion, are often invoked to explain this link (e.g. Granato et al. 2004; Springel, Di Matteo & Hernquist 2005; Croton et al. 2006). Direct tests of such models have proved challenging, although some progress has been made in measuring the time delays between star formation and AGN activity (Schawinski et al. 2007; Wild et al. 2010), allowing a comparison to the feedback timescales predicted by the simulations.

In order to investigate the relationship between AGN and SF across modern large-scale surveys, a necessary first step is to accurately identify each process. The most commonly used methods to distinguish AGN from SF in optical spectra date back to the work of Baldwin, Phillips & Terlevich (1981, hereafter BPT) proposing the use of a number of line ratio diagrams, in particular  $[\text{O III}] \lambda 5008/\text{H}\beta$  vs.  $[\text{N II}] \lambda 6585/\text{H}\alpha$ , to establish the ionizing source powering an observed emission-line spectrum. Additional line ratio diagrams were introduced by Veilleux & Osterbrock (1987).

Subsequent advances in photoionization modelling, combined with the large datasets provided by the Sloan Digital Sky Survey (SDSS; York et al. 2000), have allowed more quantitative BPT-based classifications to be made. In particular, diagnostic lines were defined in the BPT plane by Kewley et al. (2001) and Stasińska et al. (2006), based on photoionization modelling, while Kauffmann et al. (2003) presented an empirical classification based on a large sample of galaxies from the SDSS. Kewley et al. (2006) further extended these schemes by defining the region between the Kewley et al. (2001) and Kauffmann et al. (2003) lines as the ‘composite’ region, in which each galaxy is expected to host both SF and an AGN. Many related diagnostic methods have been proposed that make use of a variety of line ratios, in some cases combining these with other properties of the galaxies (e.g. Diaz, Pagel & Wilson 1985; Osterbrock, Tran & Veilleux 1992; Lamareille et al. 2004; Lamareille 2010; Marocco, Hache & Lamareille 2011; Yan et al. 2011; Juneau et al. 2011).

Notwithstanding the undoubtedly success of the BPT-based diagnostic methods in separating AGN-dominated from SF-dominated galaxies, fixed boundaries and bi-modal classifications are normally involved. In practice, for a wide range of applications, we wish to quantify the contribution from each source to each galaxy, over the full range from 100 per cent AGN to 100 per cent SF, including those cases where only a weak contribution from one of the sources is present. Such measurements will prove invaluable in, for example, studies of the feedback mechanisms that relate supermassive black hole properties to those of their host galaxies, in which case a full census of SF and AGN properties will allow a far more sensitive analysis of the connection between these two sources.

In order to make possible these more sensitive measurements, we must develop techniques that incorporate all the information contained within each optical spectrum. Additionally, information from a large number of spectra within a survey can be combined and analysed as a single unit. Blind source separation (BSS) techniques process data in this way, deriving sets of component spectra that can be combined with varying weights to reconstruct each of the input spec-

tra. The most familiar BSS technique applied to astronomical spectra is principal component analysis (PCA), which has seen use for more than two decades (Mittaz et al. 1990; Francis et al. 1992; Yip et al. 2004). While the PCA-derived component spectra can be used to provide approximations to the object spectra, the interpretation of the individual component spectra themselves has only rarely proved illuminating. The more ambitious goal is to generate component spectra that relate to the underlying physical constituents within a galaxy which can be analysed using standard techniques to determine the physical conditions contributing to the individual components.

More recently, other BSS techniques have been applied to the analysis of UV/optical spectra, including independent component analysis (ICA; Lu et al. 2006) and non-negative matrix factorisation (NMF; Blanton & Roweis 2007; Allen et al. 2011). Here we present an application of mean field independent component analysis (MFICA), a BSS technique previously unused in astronomy, to the analysis of SDSS spectra. MFICA is applied to a sample of narrow emission-line galaxies, generating a small number of component spectra that, along with a corresponding set of weights, can be used to reconstruct the spectrum of each object in the sample. This approach allows for the straightforward identification of spectra corresponding to pure SF and pure AGN, as well as the generation of high signal-to-noise ratio (S/N) examples of such spectra, which in turn can be analysed to determine their detailed physical properties.

The primary goal of this paper is to describe the MFICA technique and how the MFICA spectral components can be used to trace physically-significant trends, parametrized as loci, in the spectra of large samples of emission-line galaxies. We discuss our results for the SDSS sample primarily to illustrate the method and assess how well it works. In Section 2 we introduce MFICA, and in Section 3 we describe the galaxy samples used. Section 4 describes the methods used to generate component spectra, fit these components to observed spectra, and identify the regions of parameter space corresponding to SF and AGN. In Section 5 we present our results, including a preliminary investigation of the physical properties of galaxies within the SF and AGN regions. We summarise our conclusions in Section 6. Vacuum wavelengths are used throughout the paper.

## 2 MEAN FIELD INDEPENDENT COMPONENT ANALYSIS

Blind source separation (BSS) techniques are used to rewrite a data matrix,  $\mathbf{V}$ , as the product of a set of components,  $\mathbf{S}$ , and weights,  $\mathbf{A}$ :

$$\mathbf{V} = \mathbf{AS}. \quad (1)$$

In the context of this work,  $\mathbf{V}$  is an  $n \times m$  array of flux measurements for  $n$  different galaxies at  $m$  wavelengths,  $\mathbf{S}$  is an  $r \times m$  array of the  $r$  component spectra over the same wavelengths, and  $\mathbf{A}$  is an  $n \times r$  array of the corresponding weights for each galaxy. For any individual galaxy, the observed spectrum is written as a linear combination of the  $r$  components. In the case that  $r < n$ , the equality in equation 1 is an approximation, and the product  $\mathbf{AS}$  can be viewed as a reconstruction of the original data. The choice

of  $r$  depends on a number of factors, including the expected nature of the components, the S/N of the input data, and the particular purpose of the analysis.

Mean field independent component analysis (MFICA; Højen-Sørensen et al. 2002; Opper & Winther 2005) is a BSS technique that produces a small number of components that can be used to provide reconstructions of the individual input spectra. MFICA imposes a prior on the components,  $P(\mathbf{S})$ , and combines  $P(\mathbf{S})$  with the error in the reconstructions to maximize the likelihood of the parameters:

$$P(\mathbf{V}|\mathbf{A}, \Sigma) = \int d\mathbf{S} P(\mathbf{V}|\mathbf{A}, \Sigma, \mathbf{S}) P(\mathbf{S}), \quad (2)$$

where

$$P(\mathbf{V}|\mathbf{A}, \Sigma, \mathbf{S}) = (\det 2\pi\Sigma)^{-\frac{N}{2}} e^{-\frac{1}{2}\text{Tr}(\mathbf{V}-\mathbf{AS})^T \Sigma^{-1} (\mathbf{V}-\mathbf{AS})}, \quad (3)$$

where  $N$  is the number of input spectra, and  $\Sigma$  is the noise covariance.  $\Sigma$  does not need to be specified in advance, and is calculated from the data along with  $\mathbf{A}$  and  $\mathbf{S}$ . The parameters  $\mathbf{A}$  and  $\mathbf{S}$  provide a full description of the noise-free spectra, while  $\Sigma$  describes the noise in the observations. In this work,  $\Sigma$  is taken to be a scalar. In essence, MFICA derives a combination of  $\mathbf{A}$ ,  $\mathbf{S}$  and  $\Sigma$  that combine to explain the input data  $\mathbf{V}$ , while preferentially selecting values for the individual pixels in  $\mathbf{S}$  that maximize the chosen  $P(\mathbf{S})$ . Note that unlike many ICA techniques, MFICA does not address the issue of statistical independence.

The prior  $P(\mathbf{S})$ , which can in principle take almost any form, can be used to place constraints on the components. Restrictions can also be placed on the mixing matrix,  $\mathbf{A}$ . In particular,  $\mathbf{A}$  and  $\mathbf{S}$  can both be constrained to be non-negative; such a constraint is appealing in the context of spectroscopic observations where the physical emission signatures are expected to obey such a restriction naturally.

### 3 GALAXY SAMPLE

SDSS DR7 (Abazajian et al. 2009) galaxy samples at redshift  $z \simeq 0.1$  provide large numbers of spectra, with moderate S/N, covering a restframe wavelength interval that includes  $[\text{O II}] \lambda 3728$  in the blue, through to  $[\text{Ar III}] \lambda 7137$  in the red. A narrow redshift interval at  $z \simeq 0.1$  was thus chosen for the application of MFICA to investigate the properties of narrow emission-line galaxies.

More specifically, a large sample of SDSS-classified galaxies was selected with redshifts  $0.10 \leq z < 0.12$ .<sup>1</sup> The redshift range is sufficiently broad that a large sample of  $\sim 10^4$  galaxies is available, while retaining a large common rest-frame wavelength range for analysis. The spectra were also required to have at least 3800 ‘good’ pixels, defined as those for which the SDSS noise array is non-zero, and an  $r$ -band S/N of  $15.0 \leq \text{SN.R} < 30.0$ .

Emission-line galaxies were selected to have positive equivalent width (EW), indicating emission, for each of  $\text{H}\beta$ ,  $[\text{O III}] \lambda 5008$ ,  $\text{H}\alpha$  and  $[\text{N II}] \lambda 6585$ , with  $\text{S/N} \geq 5.0$  for the flux measurements of  $\text{H}\beta$  and  $[\text{N II}] \lambda 6585$ . The sample was

<sup>1</sup> Objects in the range  $0.111 \leq z < 0.116$  were discarded, because of the coincidence of the strong  $5578.5 \text{ \AA}$  sky-line with rest-frame  $[\text{O III}] \lambda 5008$  in the galaxies.

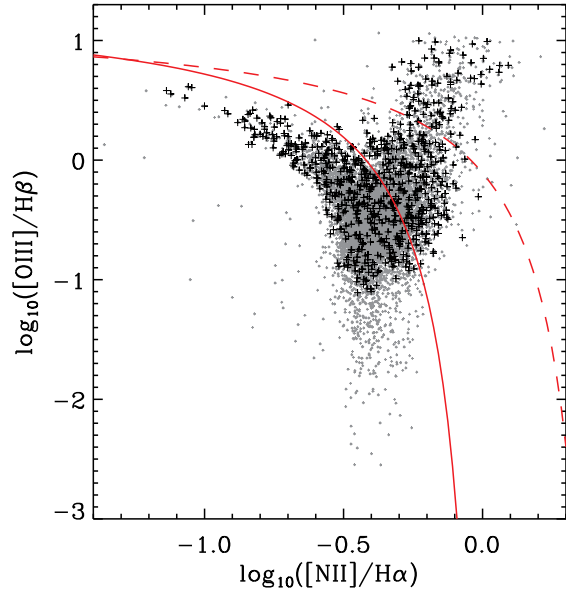


**Figure 1.** Positions of the input samples in the  $[\text{O III}] \lambda 5008/\text{H}\beta$  vs.  $[\text{N II}] \lambda 6585/\text{H}\alpha$  BPT plane. Small grey points represent the complete emission-line galaxy sample, while large black points represent those galaxies used to generate the emission-line components. The solid and dashed red lines represent the classification curves defined in Kauffmann et al. (2003) and Kewley et al. (2001), respectively.

restricted to objects with an  $\text{H}\alpha$  width  $1.9 \text{ \AA} \leq \sigma_{\text{H}\alpha} < 3.5 \text{ \AA}$ , and objects with a visually-detected broad component to their  $\text{H}\alpha$  emission were removed. The resulting sample consists of galaxies with emission lines detected at moderate S/N, and velocity widths in the interval  $\simeq 120 - 330 \text{ km s}^{-1}$ , i.e. including  $L^*$  and brighter galaxies. Their positions in the  $[\text{O III}] \lambda 5008/\text{H}\beta$  vs.  $[\text{N II}] \lambda 6585/\text{H}\alpha$  BPT plane are shown by the small grey points in Fig. 1.

A sample of galaxies without emission lines was selected from those with  $\text{H}\alpha$  detected in absorption with  $\text{S/N} \geq 3.0$  and no detected emission in  $[\text{O II}] \lambda 3728$  or  $[\text{O III}] \lambda 5008$ . A slightly broader redshift range,  $0.09 \leq z < 0.13$ , was used to increase the number of objects.

Before any further processing was carried out the spectra were sky-subtracted using the algorithm presented by Wild & Hewett (2005), which greatly improves the S/N at observed wavelengths  $> 7200 \text{ \AA}$ . All spectra were corrected for Galactic dust reddening using the  $E(B-V)$  measurements from Schlegel, Finkbeiner & Davis (1998) and the Milky Way extinction curve of Cardelli, Clayton & Mathis (1989).

The generation of components requires an accurate correction to rest-frame wavelengths, and is sensitive to sub-pixel errors in this correction. For the emission-line galaxies, redshifts were remeasured by fitting a set of three Gaussians to the  $[\text{N II}] \lambda\lambda 6550, 6585$  and  $\text{H}\alpha$  lines, after a preliminary continuum subtraction. As the primary focus of this work is the emission line spectrum rather than the underlying continuum, the  $\text{H}\alpha$  redshift was adopted as the systemic redshift. For the galaxies without emission lines, the SDSS redshift measurements – derived by cross-correlating

the spectra with a series of templates – were used. The sky-subtracted spectra were shifted to their respective rest frames, interpolating between the SDSS pixels to ensure a precise rest-frame shift. A common rest-frame wavelength range of  $3500 \text{ \AA} < \lambda < 8100 \text{ \AA}$  was retained.

### 3.1 Sample selection for component generation

Subsets of the galaxy sample are required for the generation of the MFICA-derived ‘continuum’ and ‘emission-line’ components. The number of spectra required depends on the number of components present in the object population and the S/N of the spectra.

The continuum components were derived using a modest-sized sample of 170 spectra. This sample size is adequate because only a few such components were being sought (Section 4.1). The galaxies were selected to include an approximately even spread in continuum colours between blue and red, i.e. between young (post-starburst) and old (K-giant dominated) stellar populations.

The galaxy emission-line properties exhibit a greater variation, requiring a somewhat larger sample of galaxies. The first stage in their selection was to place the objects in a classical  $[\text{O III}]/\text{H}\beta$  vs.  $[\text{N II}]/\text{H}\alpha$  BPT diagram. Galaxies were then selected with probability inversely proportional to the local density of galaxies in the BPT diagram, producing a sample evenly populating the occupied portion of the diagram. Application of somewhat tighter constraints on the spectrum S/N ( $16.0 \leq \text{SN}_R < 23.0$ ) and the  $\text{H}\alpha$  emission-line width ( $1.9 \text{ \AA} \leq \sigma_{\text{H}\alpha} < 3.0 \text{ \AA}$ ) resulted in a sample of 727 galaxy spectra. Their positions in the  $[\text{O III}]/\text{H}\beta$  vs.  $[\text{N II}]/\text{H}\alpha$  BPT plane are shown by the large black points in Fig. 1. The original sample consisted of 730 galaxies but, following visual inspection, three galaxies with significantly dust reddened continua were removed. The presence of dust reduces the observed flux by a wavelength-dependent factor; although the MFICA analysis is able to account for moderate levels of dust, the most extreme objects can no longer be described accurately by equation 1 and so are not included in the component generation.

All the spectra used in the component generation were normalised according to their median flux, to prevent a small number of bright galaxies from dominating the components.

## 4 METHOD

MFICA was used to generate components from subsets of the SDSS sample, and these components were then fitted to the full sample of galaxies in order to study their continuum and emission-line properties. The analysis is described in detail in the following subsections; a brief overview is given here. First, a set of five continuum components was generated from a combination of galaxies with and without detected emission lines (Section 4.1). The components were constructed in such a way as to avoid contamination by emission lines, allowing them to be used to reconstruct and subtract the stellar continuum in SDSS galaxy spectra. Subtracting the continuum in this manner allows us to isolate each galaxy’s emission-line spectrum with minimal contamination from underlying stellar absorption features.

Recognising the importance of accurate continuum subtraction in order to measure weak emission-line fluxes, a series of tests that probe that accuracy of the MFICA-based continuum reconstructions are described in Section 4.2. The continuum-subtracted spectra were then used to generate a set of five MFICA components that can be combined together to describe the emission line spectrum of any galaxy, including both AGN and SF galaxies (Section 4.3). The individual components do not represent distinct physical sources; rather, they are high S/N representations of spectroscopic traits that appear in galaxy spectra, and which include weaker emission lines that are now largely free of contamination by the underlying galaxy.

The five continuum and five emission-line components were then fitted to each individual galaxy spectrum in the full sample (Section 4.4). The results of this fitting allow us to characterise the emission-line properties of each galaxy in a five-dimensional space, independent of the continuum properties. Finally, Section 4.5 describes the identification of two loci of galaxies running through this five-dimensional space. One locus is identified with SF galaxies, and the other with AGN. The position of a galaxy within one of these loci is determined by its emission-line properties, and hence by the underlying physical properties of that particular SF or AGN galaxy.

### 4.1 Generating continuum components

In principle, given enough galaxy spectra of extremely high S/N and resolution, a BSS analysis should produce components that correspond to stellar spectral types that make up loci of different ages and metallicities in a Hertzsprung-Russell diagram. More realistically the goal for spectra of the quality in the SDSS is the identification of components that represent current star formation (O/B-star dominated), intermediate age (post-starburst, A-star dominated) and old (K-giant dominated), possibly with some additional age discrimination for the intermediate age star-formation signatures.

Emission-line galaxies on their own are unsuitable for deriving continuum components as the emission lines coincide with important features in the underlying stellar spectrum. This problem is particularly pronounced for the Balmer series lines, which are seen as strong absorption features in a range of main sequence stars. However, galaxies with no emission lines also produce unsatisfactory continuum components, as they do not include significant contributions from young O/B stars. In general, a sample that does not include a significant contribution due to star formation of all ages will not allow a BSS analysis to generate components that successfully reconstruct the full range of star-formation ages.

Here, such limitations affecting the identification of continuum components representing all star-formation ages were circumvented by using a mixed sample of galaxies with and without emission lines. First, a set of 20 emission-line galaxies, with particularly strong contributions to their continua from young stars, was selected using a preliminary MFICA analysis. A set of two MFICA components, which were very similar in form to the top two components in Fig. 2, was generated from the 170 galaxies without emission lines, and fitted to the 727 galaxies with emission lines. The

20 selected were those with the highest fractional contribution from the component corresponding to a young stellar population. These 20 galaxies were added to the sample of 170 galaxies without emission lines. The selection of galaxies with strong young-star contributions allowed a significant signal from such stars to be included in the sample with only a small number of emission-line galaxies, ensuring the great majority of galaxies in the sample still had no detected emission lines.

A set of seven components was generated from the mixed sample, using the exponential prior:

$$P(S) = \eta \exp(-\eta S) \Theta(S), \quad (4)$$

where  $\Theta(S)$  is the Heaviside step function and  $\eta$  is a dimensionless parameter, taken in this case as  $\eta = 1$ . This prior was selected as it is zero for negative values of  $S$ , so it produces non-negative component spectra, suitable for the characterisation of emission sources. Provided this condition is satisfied, the resulting components do not depend strongly on the form of the prior. The seven components could be cleanly divided into three that were dominated by the stellar continuum and four that were dominated by the emission lines. The emission-line components were not used in the following analysis – the method described in Section 4.3 produced emission-line components that could more easily be analysed, and at higher S/N – but they played the role of filtering out virtually all the emission-line signal, leaving the three continuum components almost entirely free of contamination by emission lines.

The number of components generated at this point was chosen to provide physically meaningful continuum components with a clean separation from the emission-line components. Generating fewer components causes some components to show a combination of continuum and emission-line signatures, rather than being dominated by one or the other. Generating a greater number of components from this sample causes the continuum signal to be spread over more components in such a way as to obscure the clear physical interpretation discussed below, while providing only a minimal improvement in the accuracy of the resulting reconstructions. The choice of seven components was made after inspecting the results from a range of numbers of components.

The performance of the MFICA in terms of the degree of cross-talk between components is impressive. However, the presence of the very high-contrast, narrow emission lines, combined with the limited S/N of the galaxy spectra, means that some low-level contamination of the continuum components by residual emission features is present. Specifically, two of the three continuum-dominated components showed some contamination, primarily at the location of the strongest emission lines. The regions of contamination were identified by visual inspection. A linear interpolation was then applied to produce the final continuum components. The parameters used in the interpolation are listed in Table 1; for each emission line the continuum between  $\lambda_{\min}$  and  $\lambda_{\max}$  was set by interpolating between the median flux levels in the  $N_{\text{pix}}$  pixels on either side of the region.

The top three spectra in Fig. 2 show the original components, as well as the results after interpolation. The three components can be identified with old, intermediate and young stellar populations (dominated by K, A and O stars

**Table 1.** Parameters used to interpolate over features in continuum components.

Component	Feature	$\lambda_{\min}$ (Å)	$\lambda_{\max}$ (Å)	$N_{\text{pix}}$
2	[O III]	4955.1	4967.6	15
	[O III]	5000.9	5012.5	15
	H $\alpha$	6563.7	6568.3	1
	[N II]	6578.8	6589.5	1
	[S II]	6715.1	6736.7	15
3	Ca K	3927.8	3939.6	15
	H $\beta$	4836.7	4892.7	15
	H $\alpha$ +[N II]	6544.1	6591.0	15
	[S II]	6704.2	6719.7	15

respectively), although the third of these components is relatively noisy. The O star component also shows an increase in flux towards the red from a population of red supergiants, formed by the rapid evolution of the most massive main sequence stars.

Although these three continuum components are very successful in reconstructing the continua of observed galaxy spectra, some systematic low-level residuals remain. There are two main effects that cause these residuals. First, as a stellar population ages, its spectral energy distribution (SED) approximates a blackbody with successively lower temperatures, so its peak flux shifts to longer wavelengths. Each of the three MFICA-derived continuum components necessarily represents an average over a range of ages, whereas the SED of individual galaxies can be dominated by star formation of a particular age. Both very young and old stellar populations produce almost invariant signatures in spectra with the S/N and resolution of the SDSS; the question is essentially how much of each component is present. By contrast, the signature of intermediate-age, post-starburst, populations produces significant changes with age as the dominant stellar type evolves from late B-, through A- to early F-type stars, and the three components cannot fully reflect these changes on their own. The second effect is that the relative contributions of the three components to an individual galaxy is largely driven by the overall shape of the SED but, for example, a red SED can result from an old stellar population with little dust, or from a younger population with a higher level of dust reddening. The spectra of these two possibilities will differ in features such as the strength of the 4000-Å break and the Balmer absorption lines and, as the MFICA approach used here does not explicitly account for dust reddening, these differences are not fully described by the existing three components.

It would be possible to reduce the residuals to some extent by increasing the number of components generated at the first step described above. This approach is not followed here, for two reasons. Firstly, the resulting components can no longer be clearly identified with stellar populations of different ages, making investigations of the sort described in Section 5.1 more challenging. Secondly, a wider range of galaxies can be reconstructed by generating additional components, to be used in combination with the first three, from a sample that has a greater number of emission-line galaxies; the inclusion of such galaxies in the input sample ensures

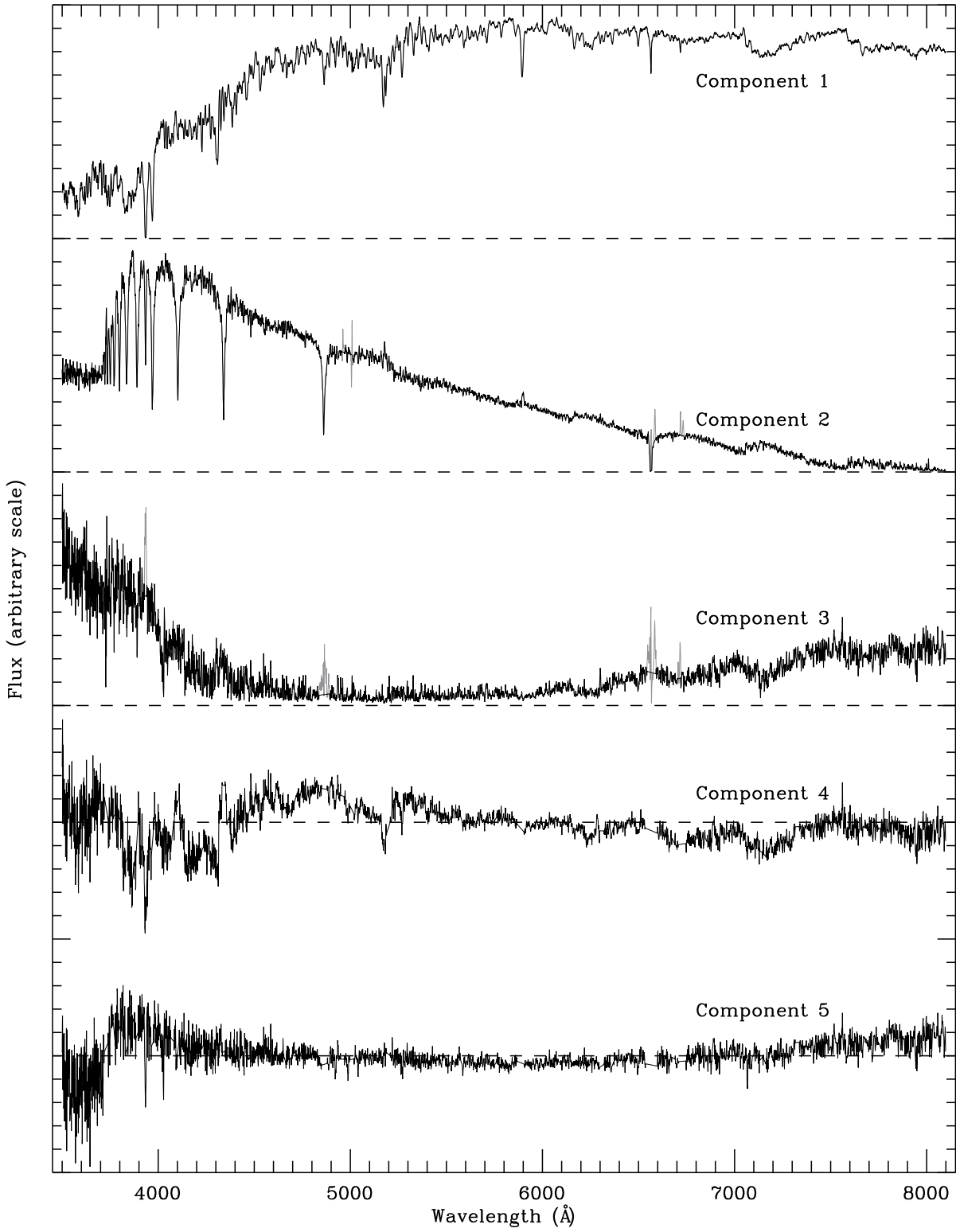


**Figure 2.** MFICA continuum components. Components are offset for clarity; dashed lines mark successive zero points. Components 1–3 were generated from a mixed sample of 170 galaxies without emission lines and 20 with emission lines; the final two ‘adjustment’ components, numbers 4 and 5, were generated from a mixed sample consisting of the same 170 galaxies without emission lines and 727 galaxies with emission lines. For components 1–3, the grey lines show the original components, while the black lines show the final versions after interpolating over a small number of narrow features.

that the components are able to describe such galaxies. We adopt this strategy here.

In order to reconstruct more accurately the spectra of galaxies covering a wide range of stellar populations and levels of dust reddening, an additional set of ‘adjustment’ components was generated, using the 170 galaxies without emission lines and all 727 with emission lines. The original three continuum components were fitted to the combined sample of 897 galaxies, with the emission-line wavelength ranges listed in Table 2 masked out, using the MFICA algorithm with the components held fixed.<sup>2</sup> After subtracting the initial three-component continuum fit, the masked ‘residual’ spectra were used to generate further MFICA components. When combined with the ‘mean’ intermediate age star-formation component, the new components allow the generation of spectra corresponding to somewhat younger and older star formation.

The positivity constraints on these additional components and their weights were dropped, and a Laplace prior was used, defined as

$$P(S) = \frac{\eta}{2} \exp(-\eta|S|), \quad (5)$$

again with  $\eta = 1$ . The Laplace prior allows both positive and negative values, making it suitable for generating components that are intended to describe deviations from a previous set of positive components. It was found that generating two additional components was sufficient to fully reconstruct the observed continua, with any further components producing no significant improvement.

The regions that had been masked out when the adjustment components were generated were interpolated over, using a simple linear interpolation, to produce the final components. The two ‘adjustment’ components are included in Fig. 2. Having removed the non-negativity constraint, these two components do not have clear physical interpretations. However, their presence does not negate the physical interpretations of the first three components, which resulted from the enforcement of non-negativity at that stage.

The continuum components were normalised such that the sum of the squares of their pixel values is equal to unity. As noted above, dust reddening is not explicitly accounted for in the reconstructions, but in practice the range of levels of reddening in the input spectra allows a similar range to be reconstructed successfully by the MFICA components. This point is discussed further in Section 5.1.

## 4.2 Accuracy of the continuum components

The effectiveness of the MFICA technique in reconstructing the underlying galaxy continua and photospheric absorption is evident from consideration of the features present in the mean and root mean square (RMS) of the galaxy minus reconstructions, for the 170 galaxies without detected emission lines (Fig. 3). The RMS is calculated after scaling the residuals by the SDSS noise arrays. The mean residual, shown in the middle panel of Fig. 3, appears to show an essentially featureless continuum with no detectable absorption

<sup>2</sup> In practice the procedure produces results almost identical to performing a minimum  $\chi^2$ -fit of the three components to each galaxy spectrum.

**Table 2.** Wavelength ranges masked when generating continuum adjustment components.

Emission line	$\lambda_{\min}$ (Å)	$\lambda_{\max}$ (Å)
[O II]	3719.5	3737.5
H $\kappa$	3748.1	3755.3
H $\iota$	3765.6	3775.1
H $\theta$	3794.8	3803.5
H $\eta$	3831.3	3840.0
[Ne III]	3865.9	3873.4
He I+H $\zeta$	3883.5	3895.4
[Ne III]+He	3964.6	3975.5
[S II]	4066.4	4081.9
H $\delta$	4098.5	4108.3
[Fe V]	4225.5	4235.5
H $\gamma$	4335.1	4347.8
[O III]	4358.8	4369.1
He I	4469.0	4476.5
[Fe III]	4655.5	4663.2
He II	4683.1	4690.9
[Ar IV]	4708.8	4716.6
[Ar IV]	4737.5	4745.5
H $\beta$	4850.1	4879.0
[O III]	4949.9	4967.7
[O III]	4997.7	5019.2
[Ar III]+[N I]	5188.9	5207.0
[Cl III]	5514.6	5523.8
[Cl III]	5534.6	5543.9
[O I]	5574.2	5583.5
[N II]	5751.4	5761.0
He I+Na D	5869.3	5904.5
[Fe VII]	6082.9	6093.1
[O I]	6296.8	6308.3
[S III]	6308.6	6319.1
[O I]	6360.2	6370.8
H $\alpha$ +[N II]	6537.0	6598.2
He I	6673.4	6686.6
[S II]	6708.2	6743.8
[Ar III]	7130.8	7143.7
[Fe II]	7150.2	7164.1
[O II]	7315.9	7337.8
[Ar III]	7746.7	7759.7

features present. Weak emission lines, including [N II], H $\alpha$ , [O III] and H $\beta$ , do however, appear to be present. The positions of these features are marked in the RMS spectrum in the bottom panel of Fig. 3.

The emission-line signature is, at first sight, unexpected given the input galaxy sample was deliberately chosen to be free of galaxies with detectable emission. Insight into the origin of the weak emission line residuals comes from the distribution of the EW of the residuals at the wavelengths of emission lines, shown in Fig. 4. The distribution consists of  $\simeq 74$  per cent of the galaxies centred on a residual H $\alpha$ +[N II] EW of  $0.8 \text{ \AA}$  ( $\simeq 1.5 \times 10^{-16} \text{ erg s}^{-1} \text{ cm}^{-2}$ ), with a tail of  $\simeq 26$  per cent of objects possessing larger positive flux residuals. The flux residuals in the tail are well in excess of the noise and a composite of the 26 per cent of galaxies with the largest residuals shows a weak, but high S/N, emission-line spectrum consistent with LINER flux ratios, with  $\log([N II]/H\alpha) = 0.13$  and  $\log([O III]/H\beta) = 0.17$ . This composite is shown in Fig. 5. For comparison, we note that Sarzi et al. (2006) found weak emission lines with H $\beta$  EW in the range 0.1–

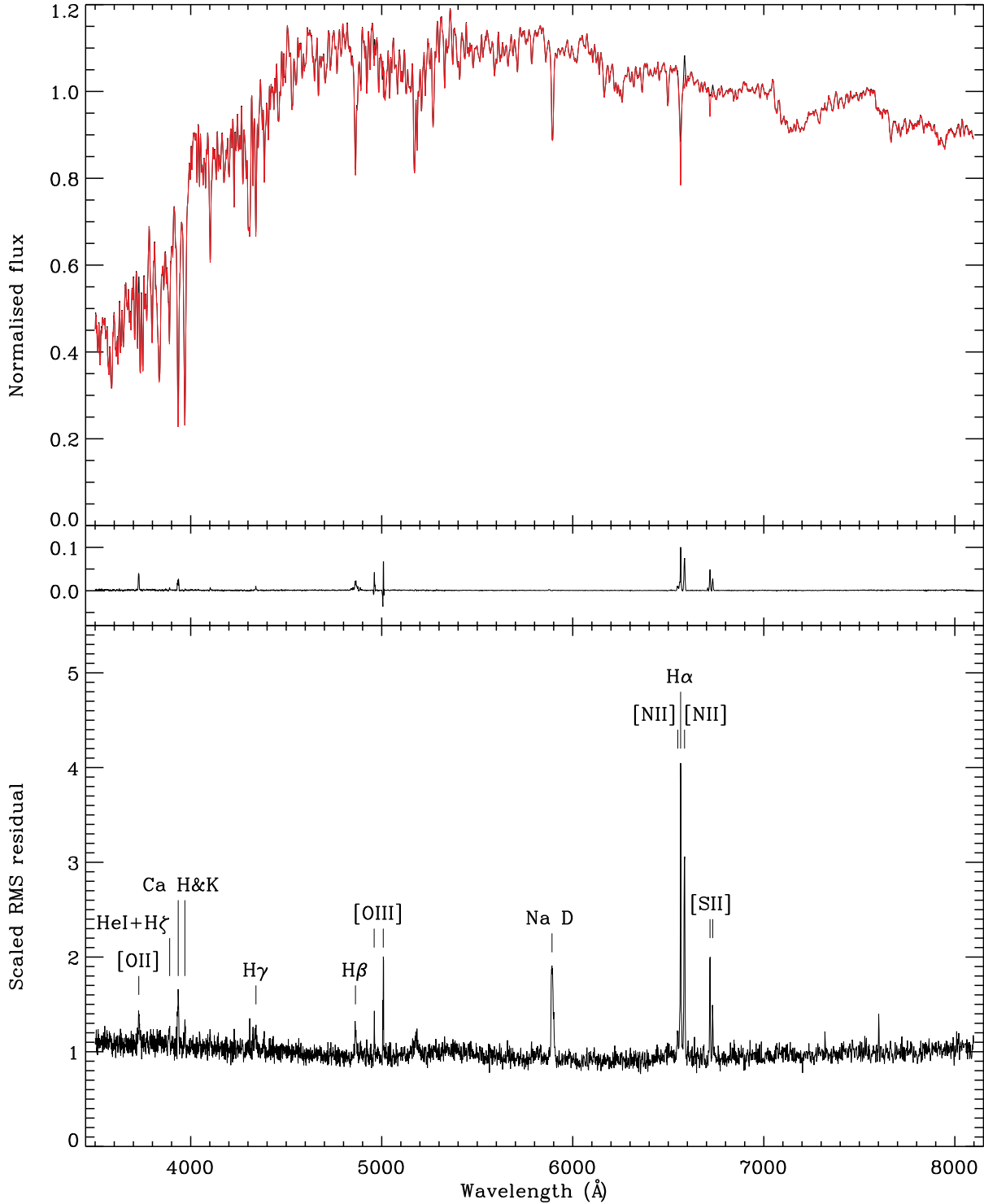


**Figure 3.** Top: mean normalised spectrum (black) of the galaxies without emission lines, and the corresponding mean MFICA reconstruction (red). Middle: mean residuals after subtracting the MFICA reconstruction. Bottom: RMS of the residuals normalised by the SDSS noise arrays. Features corresponding to known emission and absorption lines are labelled. Pixels with zero noise reported in the SDSS spectrum were removed from the RMS calculation, as was a strong artefact covering a further four pixels in one of the spectra.

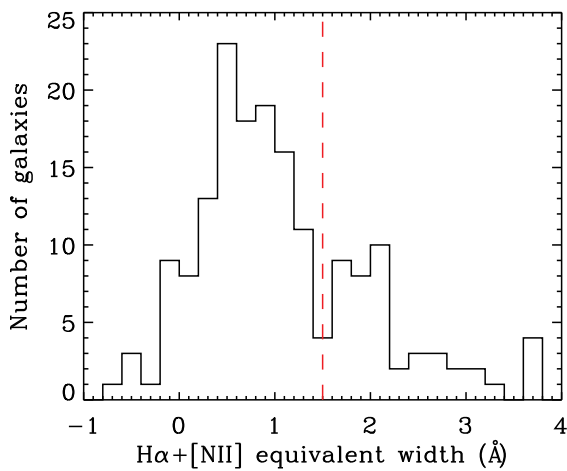


**Figure 4.** Histogram of the EW of the residuals in the  $\text{H}\alpha + [\text{N II}]$  spectral region, for the 170 galaxies without detected emission lines. Objects with  $\text{EW} > 1.5 \text{ \AA}$ , marked by the red dashed line, were included in the mean residual spectrum shown in Fig. 5.

$1.0 \text{ \AA}$  and line ratios consistent with LINERs to be common in integral field observations of early-type galaxies.

The clear emission line signature in the mean residual spectrum thus derives from the presence of a fraction of early-type galaxies that possess weak emission line signatures that elude the SDSS emission-line detection algorithm. Throughout the remainder of the wavelength range, away from the emission lines, the mean residual is, as expected, very small, not exceeding 0.5 per cent of the continuum level. The presence of the sub-sample of emission-line galaxies is also responsible for the excess RMS at the emission-line wavelengths visible in the galaxy-minus-reconstruction RMS plot.

The RMS spectrum also displays a large increase in amplitude coincident with the  $\text{Na D } \lambda\lambda 5869.3, 5904.5$  doublet and a less extreme increase coincident with the  $\text{Ca II H\&K } \lambda\lambda 3969.6, 3934.8$  doublet. The distribution of residuals for the individual galaxies in the sample (at the wavelengths of  $\text{Na D}$  and  $\text{Ca II}$ ) is centred on zero, and shows the majority to possess no significant residuals. Five of the 170 galaxies (3 per cent) show much stronger absorption than predicted by the continuum reconstructions. The absorption signature corresponds to the strong resonant transitions from species that dominate the optical spectrum of cool atomic gas in the interstellar medium of galaxies (Draine 2011). Many of the genuine early-type galaxies in the ‘continuum’ galaxy sample do not possess cool atomic interstellar medium, but the later-type galaxies (S0s and early-type spirals without current star-formation) do possess interstellar gas that manifests itself via absorption. The limited number of continuum MFICA components are unable to reproduce the additional absorption, the observational signature of which is just a small number of discrete absorption (negative) features in a small minority of the input galaxies. It would be possible in principle to generate an ‘absorption’ component using the MFICA by increasing the number of components for which the non-negativity constraint is not used, and taking care not to mask absorption

lines along with the emission lines. However, given the finite S/N of the individual spectra and very limited impact on the emission-line properties we have not pursued such a course.

The other feature due to absorption lines that appears in the bottom panel of Fig. 3 as having an unusually high RMS residual is the  $\text{Mg b}$  band at  $5180 \text{ \AA}$ . This feature is often used as an alpha-element abundance tracer. It is seen to be strong in one of the continuum adjustment components (component 4) shown in Fig. 2, suggesting that its strength has a large scatter in our sample. The increased RMS indicates that the continuum components do not fully account for this scatter. As for the  $\text{Na D}$  and  $\text{Ca II H\&K}$  features discussed above, the RMS residual at the wavelength of  $\text{Mg b}$  could in principle be decreased by increasing the number of components used. Again, we have not done so due to the very limited benefit that would be gained.

We note the absence of increased RMS in the wings of absorption features. The RMS peaks for the interstellar features discussed above are no broader than the mean absorption features themselves, while photospheric absorption features such as  $\text{Fe I } \lambda 5270$  are not visible in the RMS spectrum at all. As mentioned in Section 3, the definition of the galaxy sample via a narrow range in spectrum S/N, within a narrow redshift interval, means that the galaxies possess a restricted range of luminosity and hence mass. As a consequence, the variation in galaxy velocity dispersion is small and produces no detectable effect on the form and effectiveness of the MFICA continuum components when reproducing photospheric absorption features. Had the input galaxy sample contained a wider range of velocity dispersions, the limitations of the MFICA approach in accounting for different widths of features would have been expected to manifest itself in an increased RMS in the wings of the absorption features.<sup>3</sup>

The accuracy of the continuum reconstructions in emission-line galaxies is illustrated in Fig. 6, which shows the mean continuum fit along with the mean residual and the RMS of the residuals normalised by the noise. The sample of 727 galaxies used to produce the emission-line components (Section 4.3) was used to generate these composites. As expected there are very strong residuals at the positions of known emission lines, but in the continuum regions the RMS residuals are similar to those for the galaxies without identified emission lines, indicating the continuum reconstructions are as accurate as can be expected given the observational noise.

At the emission-line positions listed in Table 2 the accuracy of the continuum components will be impacted by the masking and interpolation used in their generation. To test the subsequent effect on the emission-line components, the continuum components were recalculated 150 times, following the procedure described in Section 4.1. For each of the 150 repeats, an additional masked region  $10\text{-\AA}$  wide, chosen at random from the regions not already masked, was

<sup>3</sup> If the continuum component definition is undertaken using a galaxy sample with a significant range of velocity-dispersion, or the continuum components are to be applied to galaxies with a significant range of velocity dispersion, galaxy spectra of continuum-components can be pre-smoothed as per the scheme for the emission lines described in Section 4.3.

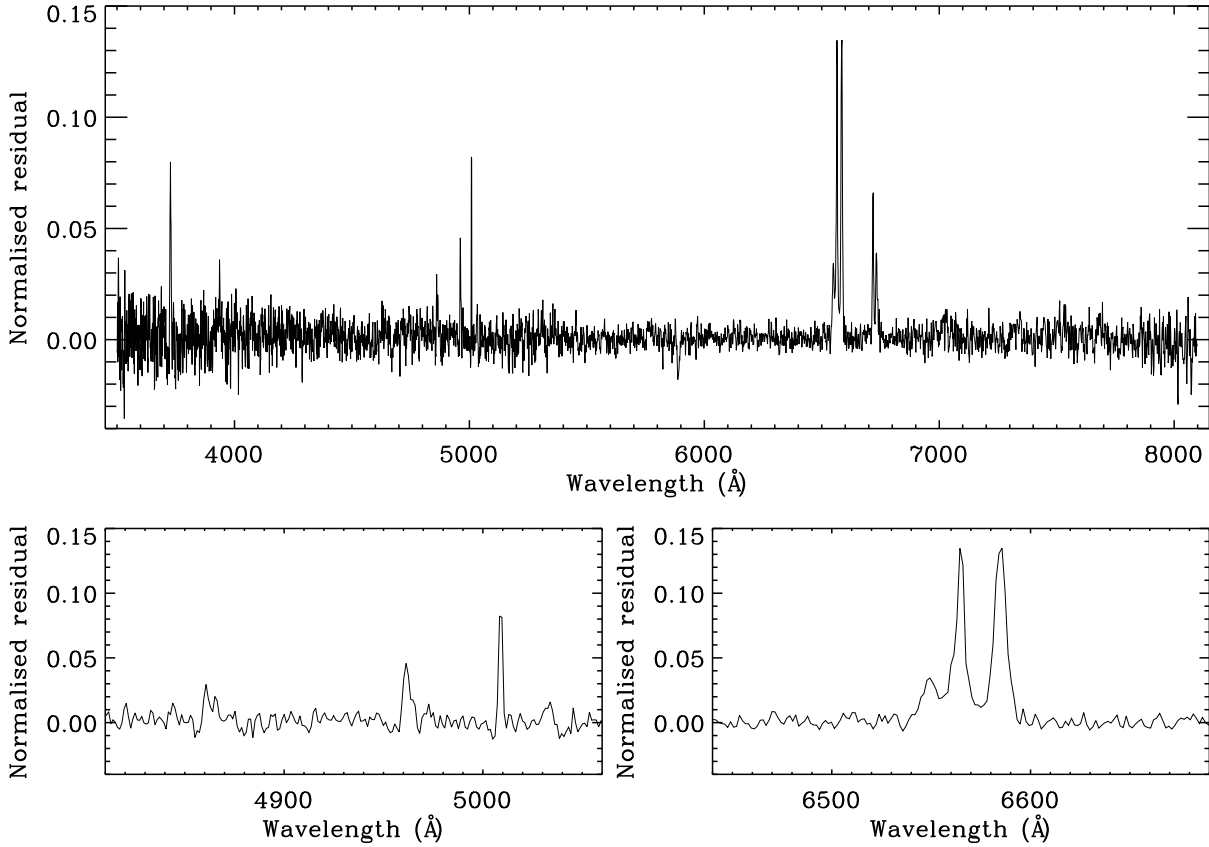


**Figure 5.** Mean residual spectrum, normalised to the median continuum level, of the 26 per cent of galaxies with the strongest residuals around H $\alpha$ , from the sample without identified emission lines. The lower panels show the regions around H $\beta$  (left) and H $\alpha$  (right) in more detail, showing LINER-like emission-line ratios.

added to the list in Table 2. The resulting continuum components were fitted to and subtracted from the sample of 727 emission-line galaxies, which were then used to generate new emission-line components following the procedure described in Section 4.3. For simplicity, the median filtering to remove the low-level positive offset described in Section 4.3 was not performed; doing so has a negligible effect on the emission line measurements. In order to measure the potential effect of the masking procedure on an emission line, four model spectra were generated from each of the 150 sets of emission-line components by combining them with weights corresponding to each end of the star-forming and AGN loci described in Section 4.5, i.e. the points s0, s2, a0 and a2 defined in that Section. ‘Median components’ were calculated by taking the median value across the 150 realisations of each component at each pixel. These median components were also combined using the same sets of weights to produce ‘median models’, which were used as a baseline against which to measure the effect of the additional masks. The change in the flux within the extra 10-Å mask, relative to the median models, was measured and normalised by the H $\beta$  flux; this change in flux was taken as a measure of the effect of the mask on the flux of a coincident emission line.

An example set of emission line components and model spectra is shown in Fig. 7. In the example shown, the region between 7235.2 and 7245.2 Å was masked out when

the fourth and fifth continuum components were generated. The resulting emission-line components, shown in the left panels of Fig. 7, are then seen to deviate from the median values in this region. As a result, the model spectra in the right panels also deviate from the median levels. However, the error introduced by this mask is very small relative to the peak flux in the components and models. Combining the  $4 \times 150 = 600$  flux measurements from all runs, the mean change in flux relative to H $\beta$  is  $2.0 \times 10^{-3}$ , with a standard deviation of  $6.3 \times 10^{-3}$ . Hence the error in the measured emission line fluxes, introduced by the masking and interpolation carried out during the continuum component generation, is constrained to be less than 1 per cent of the H $\beta$  flux.

Accurate reconstruction of the galaxy continua at locations such as the Balmer series wavelengths is of particular importance, and is made more challenging, due to the superposition of strong emission and absorption features. We test the accuracy of the MFICA Balmer absorption reconstructions by measuring the H $\beta$  absorption EW, defined using the Lick indices (Worley et al. 1994), from the continuum reconstructions for the full sample of  $\sim 10^4$  emission-line galaxies (see Section 4.4 for a description of the process of fitting the components to observed spectra). By measuring from the continuum reconstructions, which by definition do not include the emission lines, we examine the underlying ab-

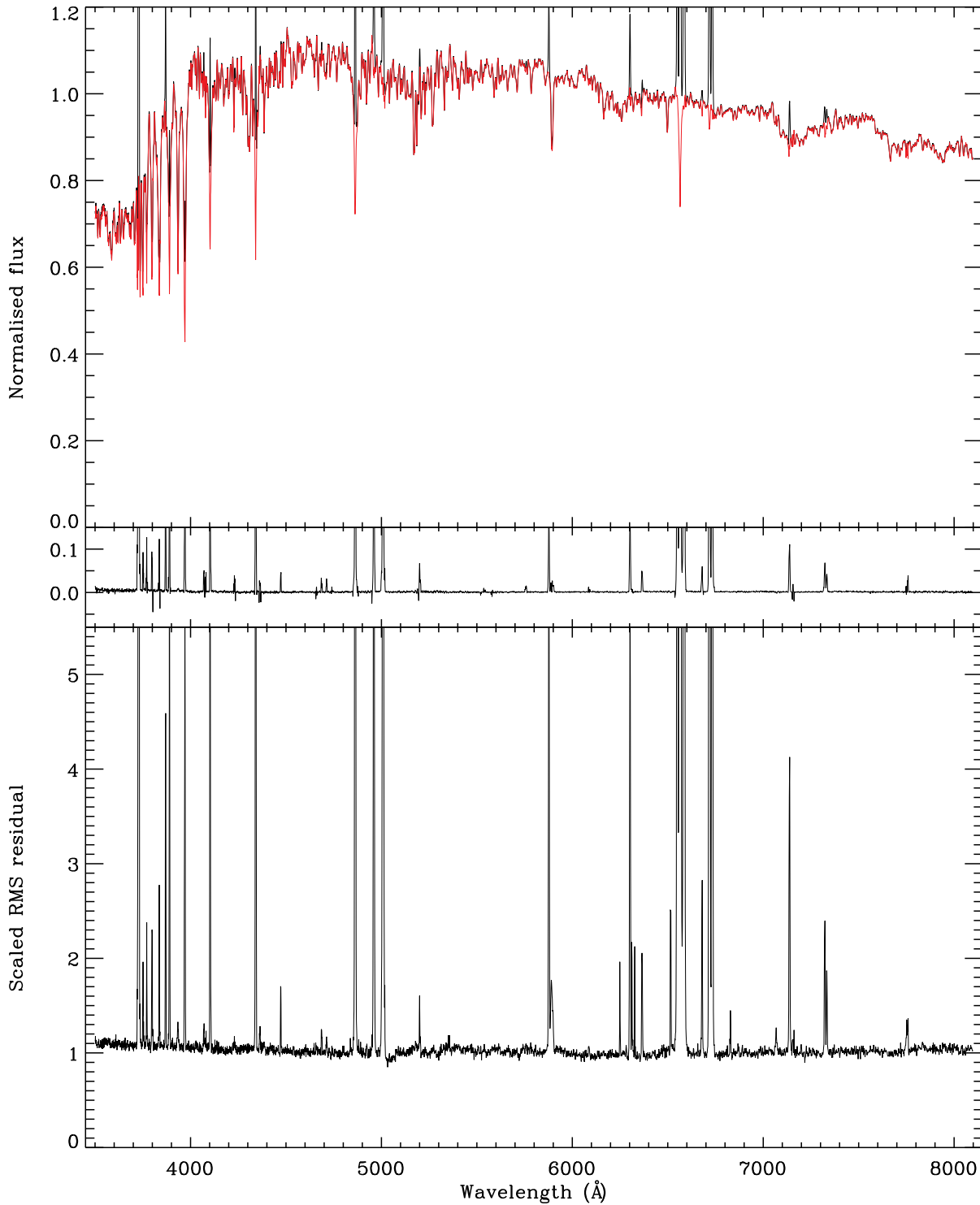


**Figure 6.** As Fig. 3, but for the 727 emission-line galaxies used to generate the emission-line components.

sorption strength as inferred by the MFICA analysis. These measurements were compared to the ‘model’ measurements in the MPA/JHU SDSS catalogue,<sup>4</sup> based on Bruzual &

Charlot (2003) stellar population models. The results are shown in Fig. 8, for the 9932 objects that appear in the MPA/JHU catalogue.

The H $\beta$  measurements are in overall agreement, with a mean offset of 0.08 Å and RMS deviation of 0.50 Å. For comparison, the mean offset between the MPA/JHU model mea-

<sup>4</sup> <http://www.mpa-garching.mpg.de/SDSS/>

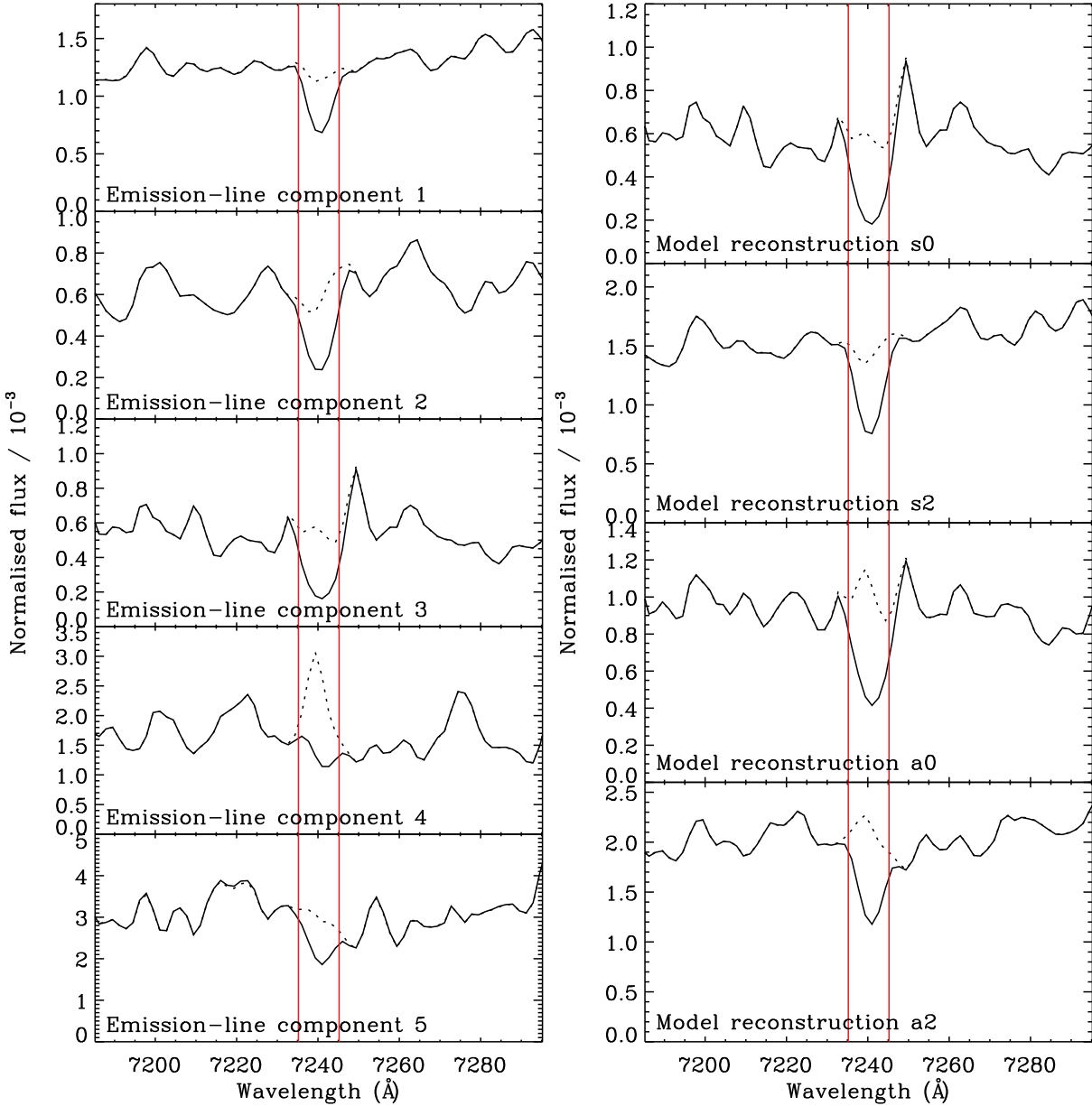


**Figure 7.** Left: Emission-line components (solid lines) generated after an extra mask covering 7235.2–7245.2 Å was included in the continuum component generation. The masked region is shown by vertical red lines. The dotted lines show the median components over all 150 repeats. Right: Model spectra (solid lines) formed from the emission-line components shown in the left panels. The median models are shown as dotted lines. The difference between the solid and dotted lines is taken as a measure of the typical error in emission line flux caused by the masking and interpolation scheme. All components and spectra are normalised relative to their peak flux. No genuine emission lines are seen in the narrow wavelength range plotted.

surements and their direct measurements after subtracting emission lines is  $-0.01$  Å, with an RMS deviation of  $0.77$  Å, indicating that the additional scatter introduced by errors in the MFICA continuum subtraction is smaller than the measurement error in an individual spectrum. Expressed as a fraction of the emission line equivalent width, as given in the MPA/JHU catalogue, the mean offset of the MFICA-based EW is 1.4 per cent with RMS deviation of 10.2 per cent. We note that the impact on the H $\beta$  emission-line fluxes will be less than this fraction, as the emission lines are typi-

cally narrower than the absorption lines in the sample used here. The good agreement between the MFICA measurements and those based on stellar population models indicates that any systematic offset in the emission-line fluxes introduced by the continuum subtraction will be small, and the additional scatter introduced is also at a low level.

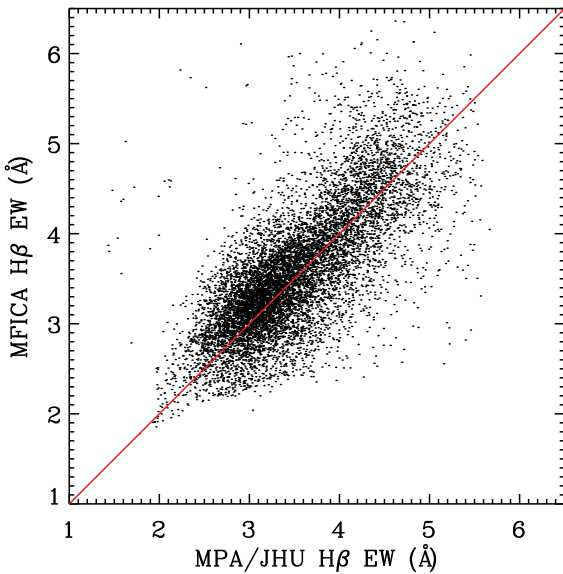


**Figure 8.** Comparison of  $H\beta$  EW, defined using the Lick indices, measured from MFICA continuum reconstructions and from the MPA/JHU catalogue, for 9932 emission-line galaxies.

#### 4.3 Generating emission-line components

The continuum components shown in Fig. 2 were fitted to and subtracted from the 727 emission-line galaxy spectra using the MFICA algorithm with fixed components, again with the wavelength ranges listed in Table 2 masked out during the fit. Preliminary tests showed that applying MFICA directly to the resulting continuum-subtracted spectra, which cover a range of emission-line widths, would produce one or more components that were dedicated to adjusting the widths of the lines. Such components have a large amount of flux in the wings of the strong emission lines, and little or none in the centres. To remove the effect of varying emission-line widths on the MFICA components, the spectra were convolved with a Gaussian kernel to produce emission lines with a fixed width of  $138 \text{ km s}^{-1}$ , corresponding to the broadest lines in the input sample. Although in doing so we effectively discard information about the width of the emission lines, this step is necessary in order to allow the components to be interpreted solely in terms of their line fluxes, and to limit the number of components required for accurate reconstructions.

The width of the Gaussian kernel for each individual galaxy was determined via a simple fit of three Gaussians to the  $[\text{N II}] \lambda\lambda 6550, 6585$  and  $H\alpha$  emission lines. Each emission-line spectrum was then convolved with a Gaussian kernel with width,  $\sigma_K = \sqrt{(138 \text{ km s}^{-1})^2 - \sigma_{H\alpha}^2}$ , where  $\sigma_{H\alpha}$  is the measured  $H\alpha$  line width in velocity space, in order to give all the spectra a  $1-\sigma$  line width of  $138 \text{ km s}^{-1}$  (2 pixels in the SDSS spectra, or  $3.02 \text{ \AA}$  at the wavelength of  $H\alpha$ ). The process is illustrated in Fig. 9, which shows an example continuum-subtracted spectrum before and after the convolution. The spectra were then renormalised to have the same total flux in the emission lines.

The MFICA algorithm itself assumes no knowledge of

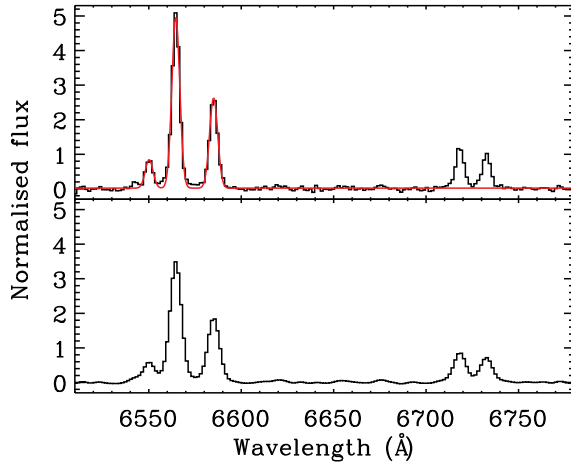


**Figure 9.** Top: continuum-subtracted narrow emission-line spectrum (black) with the Gaussian fit to the  $H\alpha$  and  $[\text{N II}]$  emission lines overplotted (red). The Gaussian fit has  $\sigma_{H\alpha} = 98 \text{ km s}^{-1}$  ( $2.15 \text{ \AA}$ ). Bottom: the same spectrum after convolving with a Gaussian kernel of width,  $\sigma_K = 97 \text{ km s}^{-1}$ , to give an output width of  $\sqrt{(98 \text{ km s}^{-1})^2 + (97 \text{ km s}^{-1})^2} = 138 \text{ km s}^{-1}$ .

the specific form of the components or the mixing matrix, but in the case of emission-line galaxies we do have some prior knowledge that can be incorporated into the analysis. In particular, for some galaxies we are able to make confident classifications based on the flux ratios of strong emission lines in a BPT diagram. Kauffmann et al. (2003) defined star-forming galaxies to be those for which

$$\log_{10} \left( \frac{[\text{O III}] \lambda 5008}{H\beta} \right) \leq \frac{0.61}{\log_{10} \left( \frac{[\text{N II}] \lambda 6585}{H\alpha} \right) - 0.05} + 1.3, \quad (6)$$

and Stasińska et al. (2006) later established that galaxies selected in this way contain no more than a 3 per cent contribution from an AGN. Thus, rather than generate components from all emission-line spectra simultaneously, it is possible to isolate a galaxy subsample whose spectra are dominated by star formation and use these to derive a set of ‘star-formation’ components. As described in Section 4.5, doing so is advantageous when considering the physical interpretation of the components.

A set of three such components was generated using only the 393 emission-line galaxies out of the sample of 727 that satisfied the Kauffmann et al. (2003) star-forming criterion. An exponential prior was used, with  $\eta = 5$ . The increased value of  $\eta$  results in a stronger distinction between high and low flux values, suppressing the flux of the components in the continuum regions, as expected for emission-line components. Increasing  $\eta$  to even greater values had negligible effect on the components. The number of components was chosen by inspecting the reconstructions of star-forming galaxies produced by different numbers of components. We found that three components are sufficient to produce reconstructions of emission-line spectra across the full range of star-forming galaxies with very high accuracy.

Additional components are necessary to describe the more extended range of emission-line properties present in

AGN spectra. The additional components were generated using the complete sample of 727 galaxies with the three star-forming components pre-specified and held fixed. The same prior was used as for the first three emission-line components. Only a further two components, making a total of five, were necessary to provide highly accurate reconstructions of essentially all spectra in the sample.

A detailed examination of the properties of the five individual MFICA-derived emission-line components was very encouraging with many weak emission lines evident at high S/N. The only apparent artefact present in each component was the presence of a very low-level positive offset, or ‘signal’, of almost constant amplitude independent of wavelength. The amplitude is extremely small, only  $\simeq 10^{-3}$  of the emission-line peaks, and well below the  $1-\sigma$  noise in the highest S/N spectra. A simple median-based filtering scheme, with a window of  $\simeq 150$  Å, was used to isolate the low-level positive signal, which was then subtracted from the component, leaving just the emission-line signatures. The emission-line components were then normalised such that the sum of their pixel values is equal to unity (the different normalisation for the continuum components in Section 4.1 was necessitated by the presence of components with mean values  $\simeq 0$ ). The resulting set of five components is shown in Figs. 10 and 11.

The two-stage process, in which the star-formation dominated galaxies were reproduced first before adding in spectra containing AGN signatures, greatly aids in the interpretation of the components. For instance, we immediately know that any galaxy with significant contributions from the fourth or fifth components contains spectral signatures distinct from those of the star-forming galaxies, indicating the presence of an AGN. This point is discussed further in Section 4.5.

An immediately obvious advantage of the MFICA component generation is that the emission-line components have a much higher S/N than any individual SDSS spectrum, allowing the identification and measurement of emission lines that are far too faint to be studied in the individual input spectra. Properties of these faint emission lines are used to investigate the physical conditions of the emitting gas in Section 5.2.

The five continuum and five emission-line components can be used in combination to characterise any SDSS narrow emission-line galaxy spectrum with suitable rest-frame wavelength coverage. The number of components required to do so is the same as was found by Yip et al. (2004) in a related PCA analysis, but the MFICA components have a number of significant advantages over their PCA counterparts. In particular, the multi-stage process by which the MFICA components were constructed provides a clear separation between emission from different physical sources, while the PCA components each contain a mixture of continuum and emission-line signals (fig. 20 of Yip et al. 2004), and have no separation between star formation and AGN contributions. The MFICA components are also able to describe a very broad range of galaxies, while the PCA components struggle to reconstruct the spectra of extreme emission-line galaxies. The separation of the components will prove particularly useful in future studies exploring the relationship between continuum and emission-line properties, as it allows the two to be characterised independently of each other.

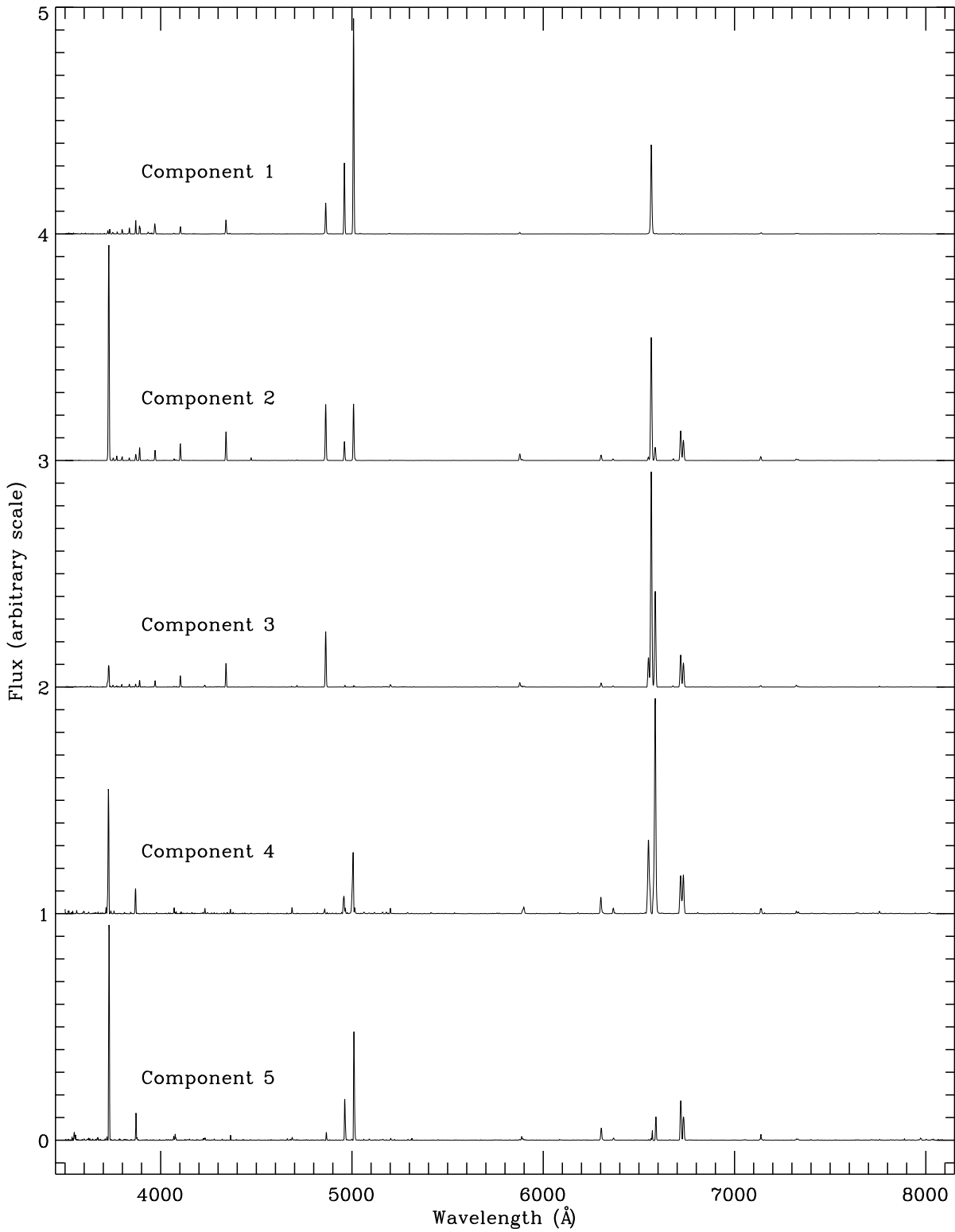
#### 4.4 Fitting components to galaxy spectra

Having derived a compact, 10-component, MFICA-generated decomposition of the carefully selected sub-sample of  $\sim 1000$  galaxy spectra the next stage in the analysis is to consider the reconstruction of a much larger number of SDSS galaxy spectra. The extended sample of spectra consisted of 10118 emission-line galaxies (Section 3), now with the full range of spectrum S/N ( $15.0 \leq \text{SN.R} < 30.0$ ) and a slightly broader range of H $\alpha$  emission-line width ( $2.0 \text{ \AA} \leq \sigma_{\text{H}\alpha} < 3.5 \text{ \AA}$ ).

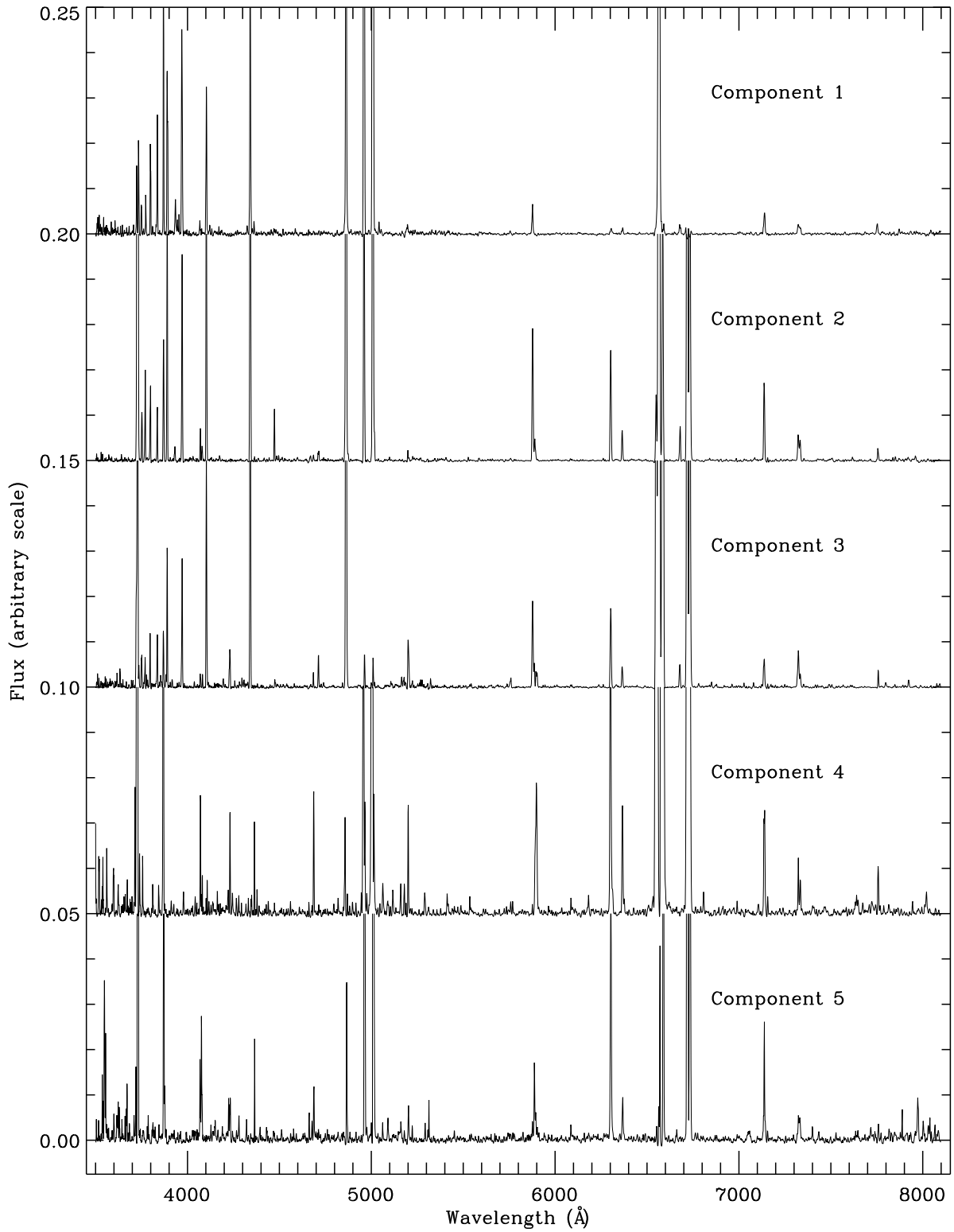
To fit the continuum components to each galaxy a  $\chi^2$  minimization was performed, using the mask defined in Table 2, with the weights for the first three components constrained to be positive. In the  $\chi^2$  minimization, and the steps described below, the SDSS noise array was used rather than the (scalar) noise covariance,  $\Sigma$ , defined as part of MFICA itself in Section 2. An accurate redshift for the emission lines is particularly important due to their rapidly varying nature as a function of wavelength. After subtracting the continuum, the redshift of the emission lines was remeasured from the H $\alpha$  line, by fitting single Gaussians to [N II]  $\lambda\lambda 6550, 6585$  and H $\alpha$ . The observed spectra were then adjusted to the new redshift, and the continuum components were refitted and subtracted. The resulting weights were normalised such that they sum to unity; in the following we denote the normalised weights by  $W_{\text{cont},i}$ . The distributions of the continuum weights are shown in Figs. 12 and 13. An alternative scheme was also tested in which the redshift of the continuum components was left as a free parameter in the fit, but doing so did not give any further improvement in the quality of the continuum subtraction. It is important to note that the MFICA-based continuum subtraction incorporates reconstructions of the stellar absorption features, allowing accurate subtractions even where these features are coincident with emission lines, such as at H $\beta$ .

Fig. 13 shows some intriguing differences between galaxies with and without emission lines. Very low values of  $W_{\text{cont},3}$  in the galaxies without emission lines suggest a lack of recent star formation, as expected. These galaxies also have very small values of  $W_{\text{cont},4}$  and  $W_{\text{cont},5}$ ; in Section 5.1 we show that this corresponds to the lowest observed levels of dust reddening. However, as these galaxies were themselves used in generating the continuum components, care must be taken when comparing their weights to those of the full sample. As expected from the way in which they were selected, the 20 emission-line galaxies used in generating continuum components 1–3 show extremely high values of  $W_{\text{cont},2}$ , and often high values of  $W_{\text{cont},3}$  as well, indicating high levels of recent or ongoing star formation. The continuum weights of the emission-line galaxies are examined in more detail in Section 5.1.

The range of emission-line width in galaxies used to define the sample from which the MFICA components were derived was deliberately constrained to have an upper limit of  $\sigma_{\text{H}\alpha} < 3.02$  Å. The rationale was to retain the maximum information, evident at relatively high spectral resolution, in the MFICA emission-line components. The SDSS-selected galaxy population as a whole includes objects with significantly broader emission-line velocity widths, although the percentage of such objects is small; for galaxies that do not possess a visible broad emission-line AGN component ap-



**Figure 10.** Final set of emission-line components. Components are offset for clarity. Components 1–3 were generated using only the 393 star-forming galaxies; components 4 and 5 used all 727 galaxies.



**Figure 11.** As Fig. 10, but showing the faint emission lines. Components are offset for clarity. The ordering of the components and the  $y$ -axis scale are the same as in Fig. 10.

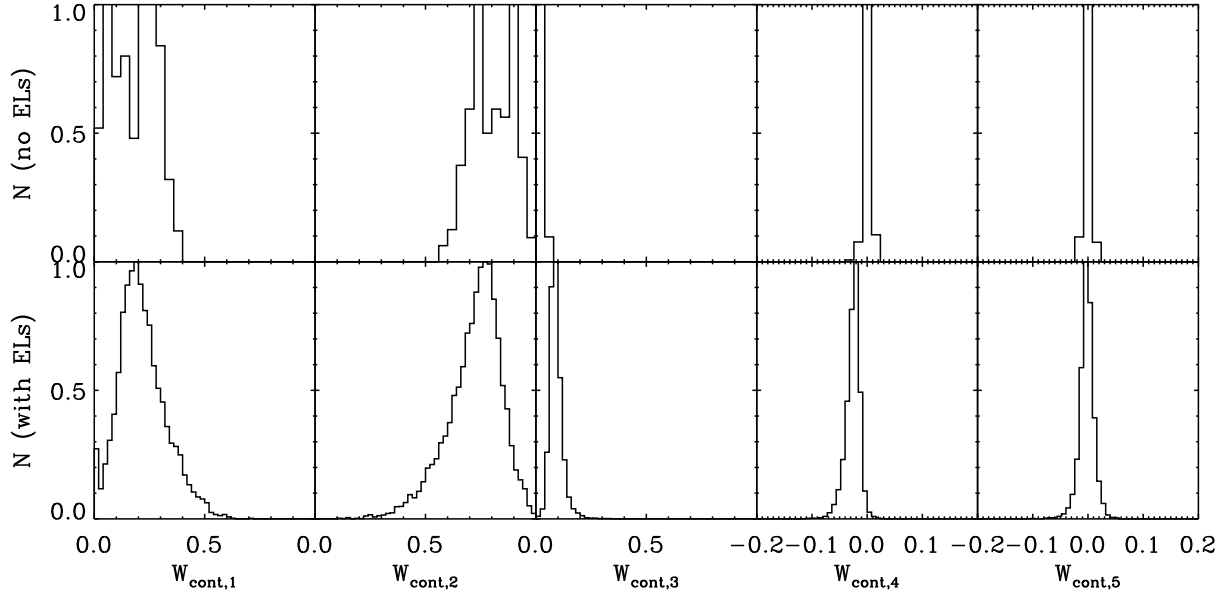


**Figure 12.** Distributions of the individual continuum component weights, each normalised to their maximum values. The upper panels are for the 170 galaxies without emission lines (ELs), which formed the bulk of the sample from which the first three continuum components were derived. The lower panels are for the full sample of 10118 emission-line galaxies.

proximately 3 per cent possess  $\sigma_{\text{H}\alpha} > 3.5 \text{ \AA}$  and well under 0.5 per cent have  $\sigma_{\text{H}\alpha} > 5.0 \text{ \AA}$ .

It is essential that the emission-line widths of individual galaxies and the MFICA components match very closely in order for an accurate decomposition to be obtained. For galaxies with  $\text{H}\alpha$  width  $\sigma_{\text{H}\alpha} < 138 \text{ km s}^{-1}$  ( $3.02 \text{ \AA}$ ), the spectra were convolved with a Gaussian kernel to produce a spectrum with  $\sigma_{\text{H}\alpha} = 138 \text{ km s}^{-1}$ , following the same procedure as described in Section 4.3. Where a galaxy possessed an  $\text{H}\alpha$  width exceeding  $138 \text{ km s}^{-1}$ , the MFICA emission-line components were convolved with a Gaussian kernel to produce components with the same emission-line width as in the galaxy. With the galaxy and component emission-line widths made equal the emission-line components were then fitted to the spectra, using a  $\chi^2$  minimization with all component weights constrained to be positive. The weights were normalised such that they sum to unity. The distributions of emission-line component weights,  $W_i$ , are shown in Figs. 14 and 15. The median values of the formal  $1-\sigma$  uncertainties are 0.004, 0.008, 0.009, 0.006 and 0.009 in each of the weights, respectively.

The emission-line components allow highly accurate descriptions of galaxies across the entire populated area in the  $[\text{O III}]/\text{H}\beta$  vs.  $[\text{N II}]/\text{H}\alpha$  plane. Median absolute deviation fractional errors in the reconstructed fluxes are 1.8 per cent in  $\text{H}\alpha$ , 7.6 per cent in  $\text{H}\beta$  and 12.7 per cent in  $[\text{O III}] \lambda 5008$ , corresponding, given the S/N of the spectra, to  $1.3\sigma$ ,  $1.8\sigma$  and  $1.2\sigma$ , respectively. Assuming Gaussian errors in the measurements of observed flux, perfect reconstructions would result in a median absolute deviation of  $0.67\sigma$  due to observational noise. Subtracting the reconstructions from the emission-line spectra removes 93 per cent of the excess RMS in the emission lines, relative to that in the continuum. Example reconstructions are shown in Fig. 16 for both pure

star-forming galaxies and those with AGN, illustrating the accuracy of the fits for a range of galaxy properties.

As the MFICA components, and hence the reconstructions, have considerably higher S/N than the individual SDSS spectra, flux measurements can be made from a reconstruction for emission lines that are too weak to be measured in the corresponding observed spectrum. However, the form of the reconstruction is itself dominated by the strong emission lines, so any measurement of weak line fluxes in an individual galaxy should be viewed as a prediction based on the properties of the stronger lines. This prediction is, in essence, an average over a number of galaxies with similar properties in their strong emission lines.

#### 4.5 Definition of star formation and active galactic nuclei loci

A primary goal of the application of the MFICA-component decomposition of the galaxy spectra is to generate a quantitative estimate of the contribution of both star-formation-related processes and any AGN that may be present to the observed spectrum. The two-stage process used to derive the emission-line components already gives important information about the interpretation of the component weights, as any galaxy with significant contributions from the fourth or fifth components has a spectrum that cannot be due to star formation alone, strongly suggesting the presence of an AGN. However, this information alone is insufficient to quantify the star-formation and AGN contributions to all galaxies, or to extract the spectral signature of these individual contributions, and a more precise MFICA-based definition of SF and AGN is required.

Star formation and AGN each produce observed emission-line spectra that display a range of properties and even ‘pure’ examples of each do not correspond to individ-

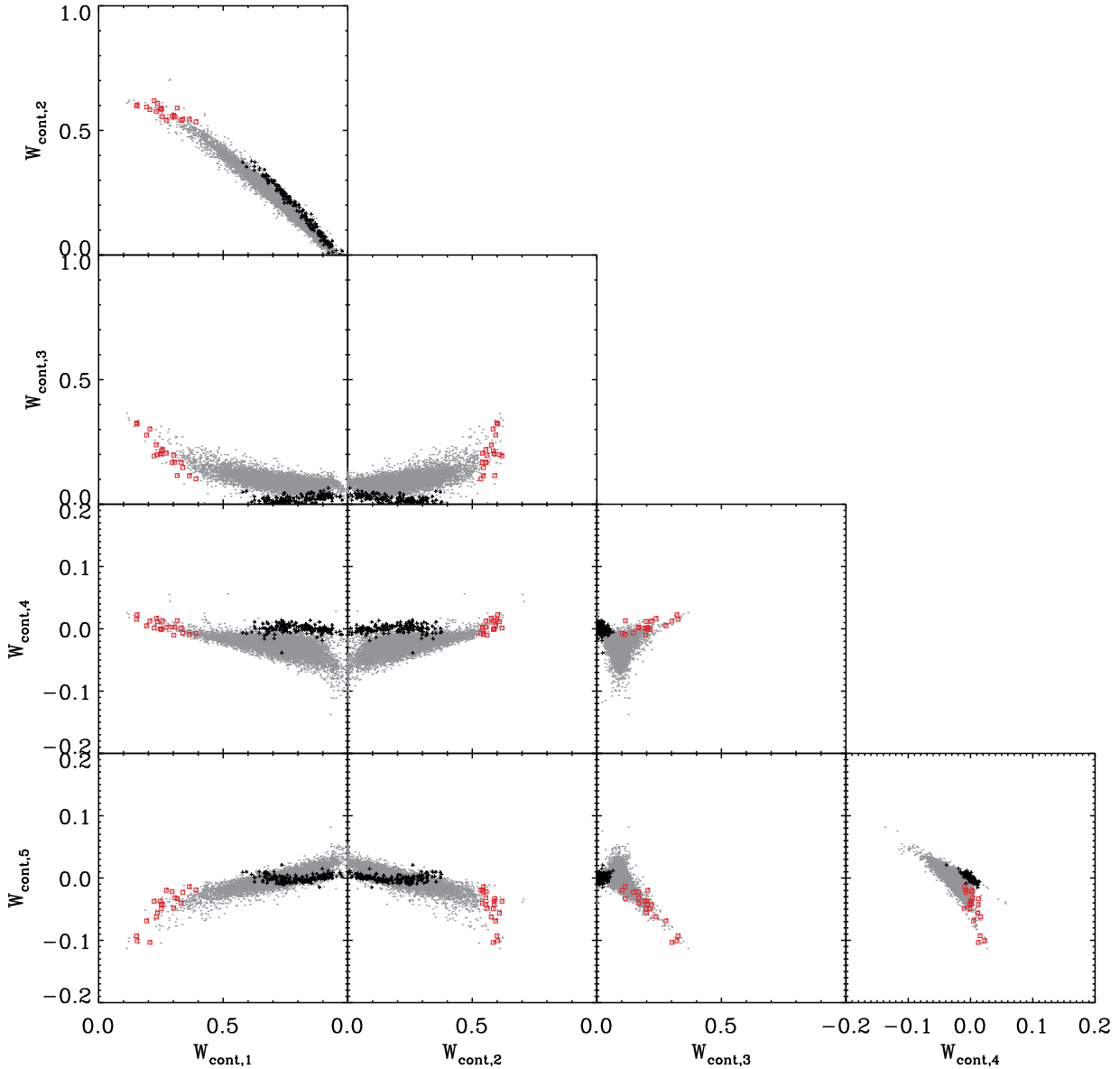


**Figure 13.** Distributions of continuum component weights. The larger black points are for the 170 galaxies without emission lines; red squares are for the 20 emission-line galaxies used when generating continuum components 1–3; smaller grey points are for the full sample of 10118 emission-line galaxies.

ual points in the five-dimensional space of MFICA emission-line component weights. Instead, more extended regions of the space are occupied by objects whose spectra arise solely from star-formation-related processes or manifestations of an AGN. In the case of star formation for example, the emission-line spectrum evolves significantly as a function of the age since a starburst and factors such as the initial mass function (IMF) of the burst and the metallicity of the gas may also contribute to the diversity of spectral properties.

The form of the distribution of star-formation- and AGN-dominated spectra in the classical BPT diagrams, together with visual inspection of the location of the galaxy spectra in the five-dimensional space of the MFICA component weights, strongly suggest that the ‘pure’ examples are

restricted to limited regions of the space of MFICA weights. A natural choice was therefore to parametrize these regions as multi-dimensional loci, using the algorithm presented by Newberg & Yanny (1997). The algorithm uses an iterative procedure to define a set of locus points that follow the centre of an extended distribution of data points. At each locus point the distribution of data points around the locus is described by an ellipse (or higher-dimensional ellipsoid).

The algorithm was implemented with  $N_{\sigma_{\text{spacing}}} = 3.0$ , no maximum distance for inclusion in the locus (see Newberg & Yanny (1997) for definitions of these parameters) and an additional requirement that at least 20 data points must exist between two locus points for an extra locus point to be inserted.

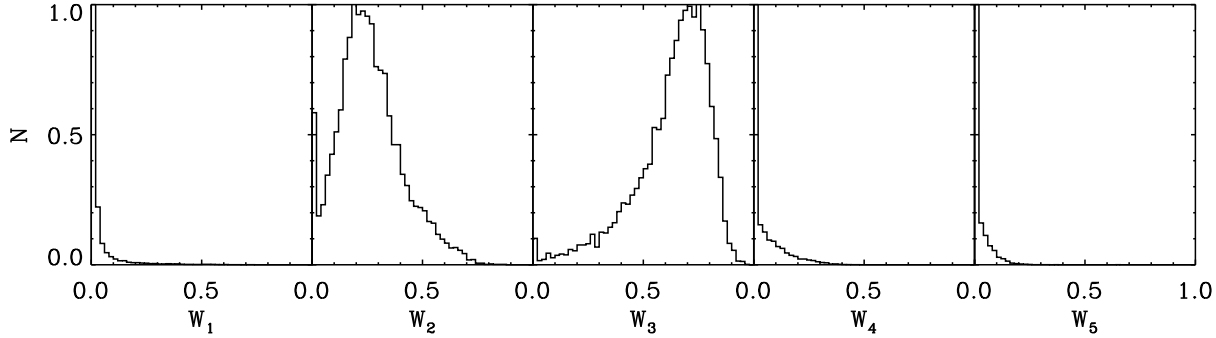


**Figure 14.** Distributions of the individual emission-line component weights, each normalised to their maximum values.

The star-formation locus was defined using the 5519 objects that satisfied the Kauffmann et al. (2003) star-forming definition. As these objects are each expected to contain no more than a 3 per cent contribution to their emission-line flux from an AGN, they can be used to explore the range of component weights corresponding to star-formation-dominated spectra. The locus was assumed to carry zero weight from the final two emission-line components and is defined only in the three-dimensional space of the first three component weights. The resulting locus is plotted in blue in Fig. 15. Moving along the length of the locus is approximately equivalent to moving along the star-formation ‘wing’ of the BPT diagram.

The corresponding AGN locus is more challenging to define, as objects selected from BPT-based definitions may contain substantial star-formation contributions. However, it can be seen in Fig. 15 that the SF locus has non-zero contributions from the second component throughout its length, other than at the extreme end, where the weight of the third component tends to unity. As such, those objects with minimal contributions from the second component can be assumed to be pure, or nearly-pure, AGN. The AGN locus was defined in all five dimensions from the 379 objects with weights  $W_2 \leq 0.05$  and  $W_4 + W_5 \geq 0.18$ . The second criterion ensures a clean separation of the star-formation and AGN loci; relaxing the criterion gives no improvement in the ability of the loci to describe observed galaxies, but greatly increases the degeneracies in the decomposition of objects into star-formation and AGN contributions, suggesting that the objects excluded by this criterion are primarily composite objects.

The AGN locus is plotted in red in Fig. 15. For each of the star-formation and AGN loci the  $1-\sigma$  radii generated by the Newberg & Yanny (1997) algorithm were multiplied by 1.5 to more fully encompass the contributing objects. The resulting ellipses, defining the transverse width of the loci at each point along their length, are included in Fig. 15.

## 5 RESULTS AND DISCUSSION

The MFICA components derived in Section 4 provide new avenues for the investigation of galaxy properties. The high S/N reconstructions that result from the components can be examined to discern the detailed physical properties of

the corresponding emission regions. Additionally, the set of weights measured for any individual galaxy acts as a compact representation of its observational properties, and hence the distributions of these weights carry information about the distributions of various properties within the galaxy sample under investigation. Although we defer a full exploration of these possibilities to future papers, we here present a brief illustration of the correlations between the MFICA continuum weights and previously-measured star formation histories, as well as preliminary results from photoionization modelling of a range of emission-line spectra.

### 5.1 Comparison with VESPA results

The clear identification of the three positive continuum components with old, intermediate and young stellar populations, respectively, allows the weights of these components within any individual galaxy to be used as a crude measure of the galaxy’s star formation history (SFH). A full development of such a technique is beyond the scope of this paper, but we present here a comparison of our results with those from a recent catalogue of SFHs, in order to demonstrate the success of the MFICA algorithm in identifying a variety of different stellar populations.

The VESPA algorithm (Tojeiro et al. 2007) derives SFHs by fitting combinations of simple stellar population models to observed galaxy spectra. The metallicity of each stellar population is also derived, along with a measurement of the overall dust content. The number of free parameters is varied according to the S/N and other properties of each individual spectrum, ensuring a robust determination of the SFH at the level of precision that is warranted by the data. Tojeiro et al. (2009) present a catalogue of VESPA-derived SFHs for the SDSS, from which we draw our comparison data. Of the 10118 galaxies in the emission-line galaxy sample, VESPA data were available for 9113; we retrieved the data for these galaxies derived using the Bruzual & Charlot (2003) stellar population models and a single-parameter dust model. The extinction law is based on the mixed slab model of Charlot & Fall (2000), characterised by the optical depth at 5500 Å,  $\tau_V^{\text{ISM}}$ <sup>5</sup>.

<sup>5</sup> Tojeiro et al. (2009) also present results using a two-parameter dust model that allows a higher level of dust in birth clouds. For

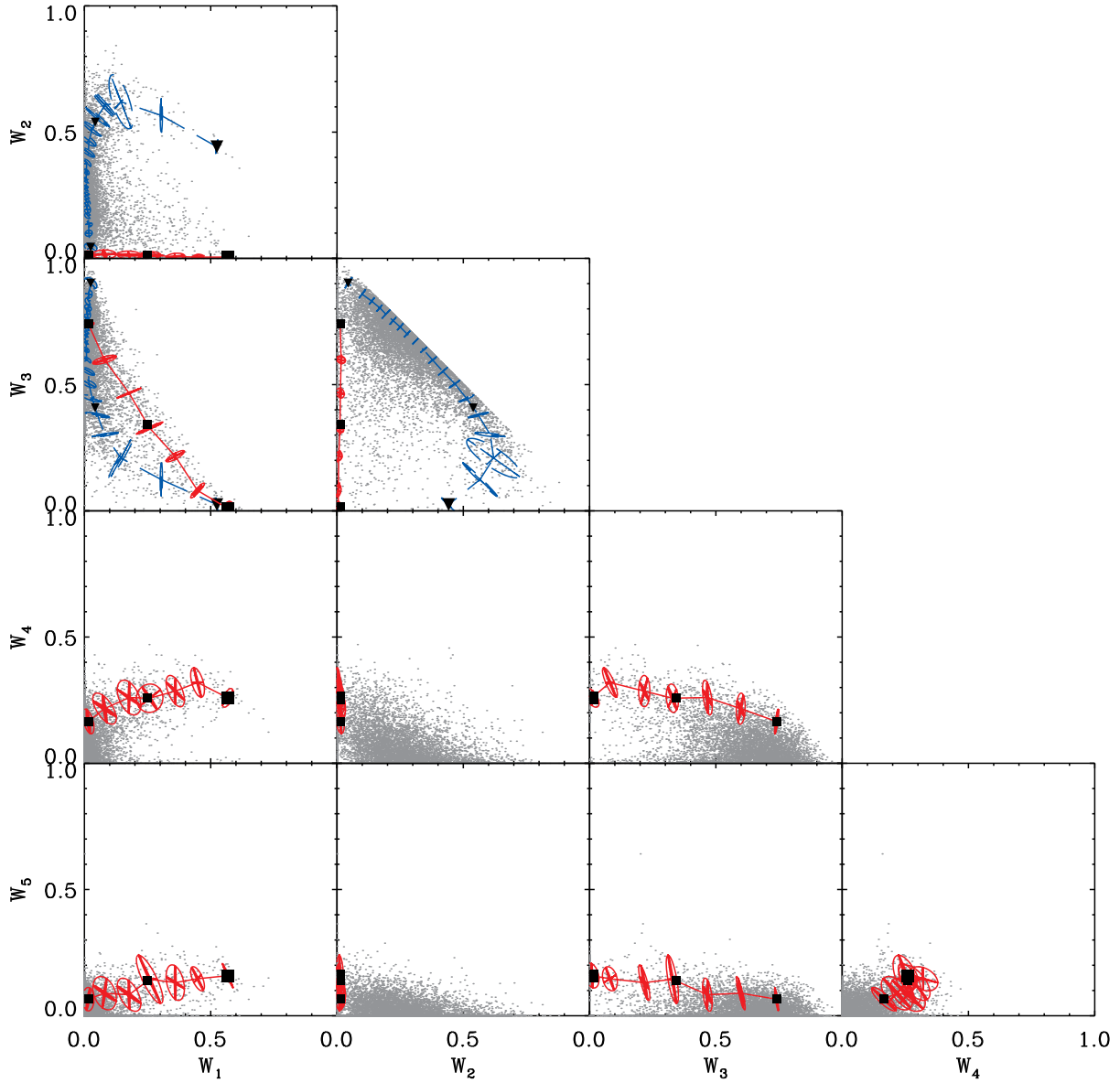


**Figure 15.** Distributions of emission-line component weights. Overplotted are the loci for SF (dashed blue) and AGN (solid red). The positions of the representative spectra are also shown for SF (triangles) and AGN (squares); larger symbols represent s2 and a2, i.e. the spectra with the highest  $[\text{O III}]/\text{H}\beta$ .

A direct comparison of the MFICA and VESPA results is shown in Fig. 17. In this figure the  $x$ -axis shows the MFICA component weight for the old stellar population (K-giant dominated) divided by the summed weights of the younger populations (O- and A-star dominated). The  $y$ -axis shows the VESPA-derived ratio of old ( $>0.42$  Gyr) to young ( $<0.42$  Gyr) stellar masses. The division at 0.42 Gyr splits the logarithmically-spaced VESPA age bins in half, and is approximately equal to the main sequence lifetime of an A-star. Only galaxies with  $\tau_V^{\text{ISM}} \leq 0.75$  are shown. Even though the figure compares a ratio of masses to a ratio of

simplicity we restrict our comparison to the single-parameter dust model here.

luminosities, there is a very strong correlation between the two.

The dust reddening explicitly included in the VESPA fit allows it to distinguish between a young dust-reddened stellar population, and an older population with little or no dust, which may have a similar overall spectral shape. In contrast, the MFICA fit does not explicitly include the effect of dust, so dust reddening is accounted for by increasing the contribution from an old, red, stellar population. This effect can be seen in Fig. 18, which shows the same data as Fig. 17 but for all values of  $\tau_V^{\text{ISM}}$ , denoted by the colour scale. The different methods by which the two algorithms account for dust results in the systematic increase in  $\tau_V^{\text{ISM}}$  that can be

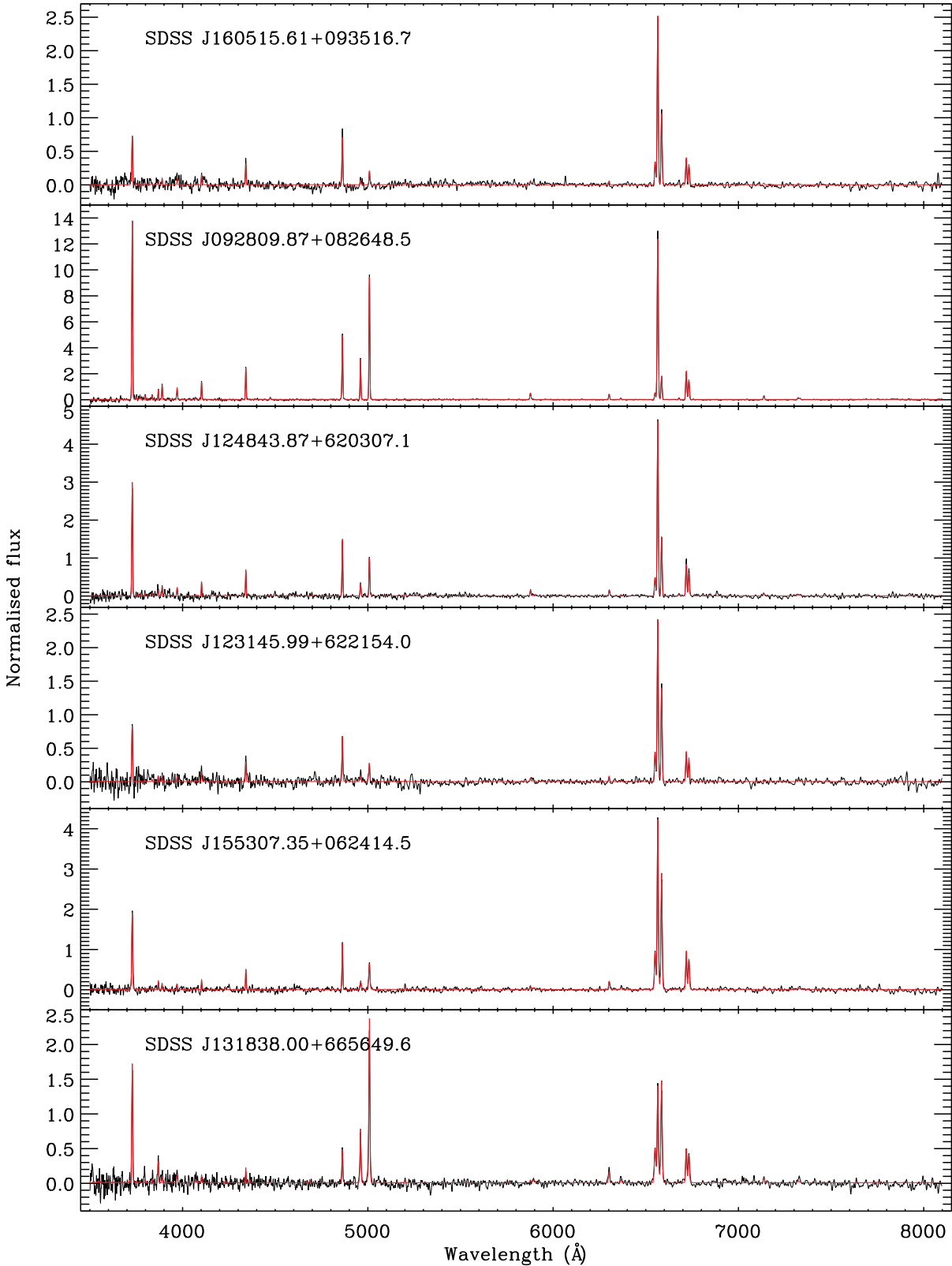


**Figure 16.** Example MFICA reconstructions of pure star-forming galaxies (top three panels) and those with AGN contributions (bottom three panels). In each panel the continuum-subtracted spectrum is plotted in black, and the MFICA reconstruction in red. The object name is given in each panel.

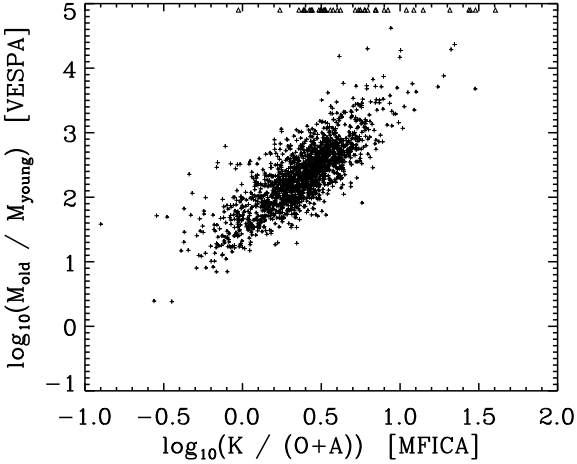


**Figure 17.** VESPA-derived ratio of old ( $>0.42$  Gyr) to young ( $<0.42$  Gyr) stellar masses, vs. ratio of MFICA weights for old (K-giant dominated) and young (O- and A-star dominated) stellar populations. Objects beyond the limits of the figure – typically because  $M_{\text{young}} = 0$  – are marked with triangles. Only those galaxies with  $\tau_V^{\text{ISM}} \leq 0.75$  are shown.

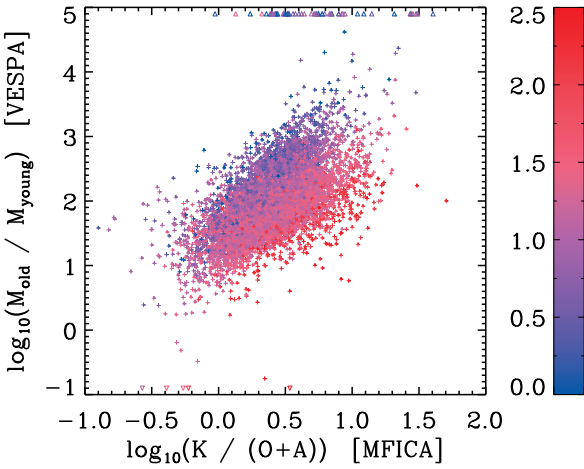


**Figure 18.** As Fig. 17, but showing galaxies with all values of  $\tau_V^{\text{ISM}}$ , as denoted by the colour scale. There is a systematic increase in  $\tau_V^{\text{ISM}}$  towards the bottom-right corner.

seen when moving to higher  $\log_{10}(K/(O+A))$  at any fixed  $\log_{10}(M_{\text{old}}/M_{\text{young}})$ .

Although the MFICA algorithm does not explicitly account for dust, it is still possible to distinguish between different levels of dust reddening by considering the full 5-dimensional distribution of component weights. As an illustration of this potential, Fig. 19 shows the MFICA weights for the two ‘adjustment’ components, with the value of  $\tau_V^{\text{ISM}}$  again denoted by the colour scale. It is clear that the position of an individual galaxy in the  $W_{\text{cont},4}$ – $W_{\text{cont},5}$  plane can be used to predict its level of dust reddening, and hence, when combined with the other component weights, the nature of its stellar populations.

Although we do not present a calibrated method for

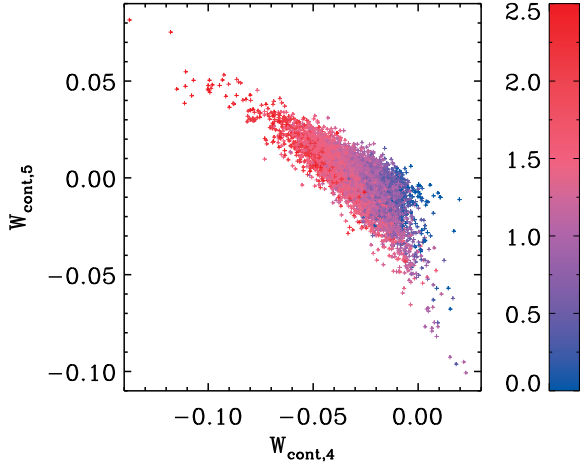


**Figure 19.** MFICA weights for the two continuum ‘adjustment’ components. Points are colour-coded according to their VESPA-derived  $\tau_V^{\text{ISM}}$  value, as in Fig. 18; there is a strong correspondence between  $\tau_V^{\text{ISM}}$  and position in the  $W_{\text{cont},4}$ – $W_{\text{cont},5}$  plane.

deriving SFHs, the strong correlations between the VESPA results and the MFICA continuum component weights illustrate the success of the MFICA technique in identifying and quantifying the contributions from stellar populations of different ages. Future studies will unlock the full potential of this technique by establishing the exact nature of the correspondence between the SFH of a galaxy and its derived MFICA weights.

## 5.2 Physical interpretation of MFICA loci

### 5.2.1 Emission line strengths

In order to explore the physical properties of galaxies within the AGN and SF loci, we generated a series of three reconstructed MFICA spectra lying along the extent of each locus. In the AGN locus, point a0 falls at a position very near to the star-forming sequence, point a2 is the opposite end of the locus and corresponds to the extreme AGN case, while point a1 is midway along the locus. Similarly, points s0, s1, s2 correspond to increasingly high ionization levels along the SF locus. The six reconstructed spectra are shown in Fig. 20, along with composite spectra of observed galaxies with similar MFICA weights. Their component weights are included in Fig. 15. Table 3 lists emission line strengths measured directly from the reconstructed MFICA spectra, and also values dereddened (using a standard Galactic reddening curve) so that  $I(\text{H}\alpha)/I(\text{H}\beta) = 2.86$ .

Compared to the results that can be obtained by simply co-adding some modest number of observed spectra, these reconstructed spectra are purer tracers of either just AGN-like properties or just star-forming-region properties, with a higher S/N and better subtraction of the background galaxies. The table illustrates the wide range of emission lines that can be measured reliably. In the following subsections we investigate the degree to which physical information is carried by the progression of emission-line properties along these loci. We note that, although table 3 includes emission

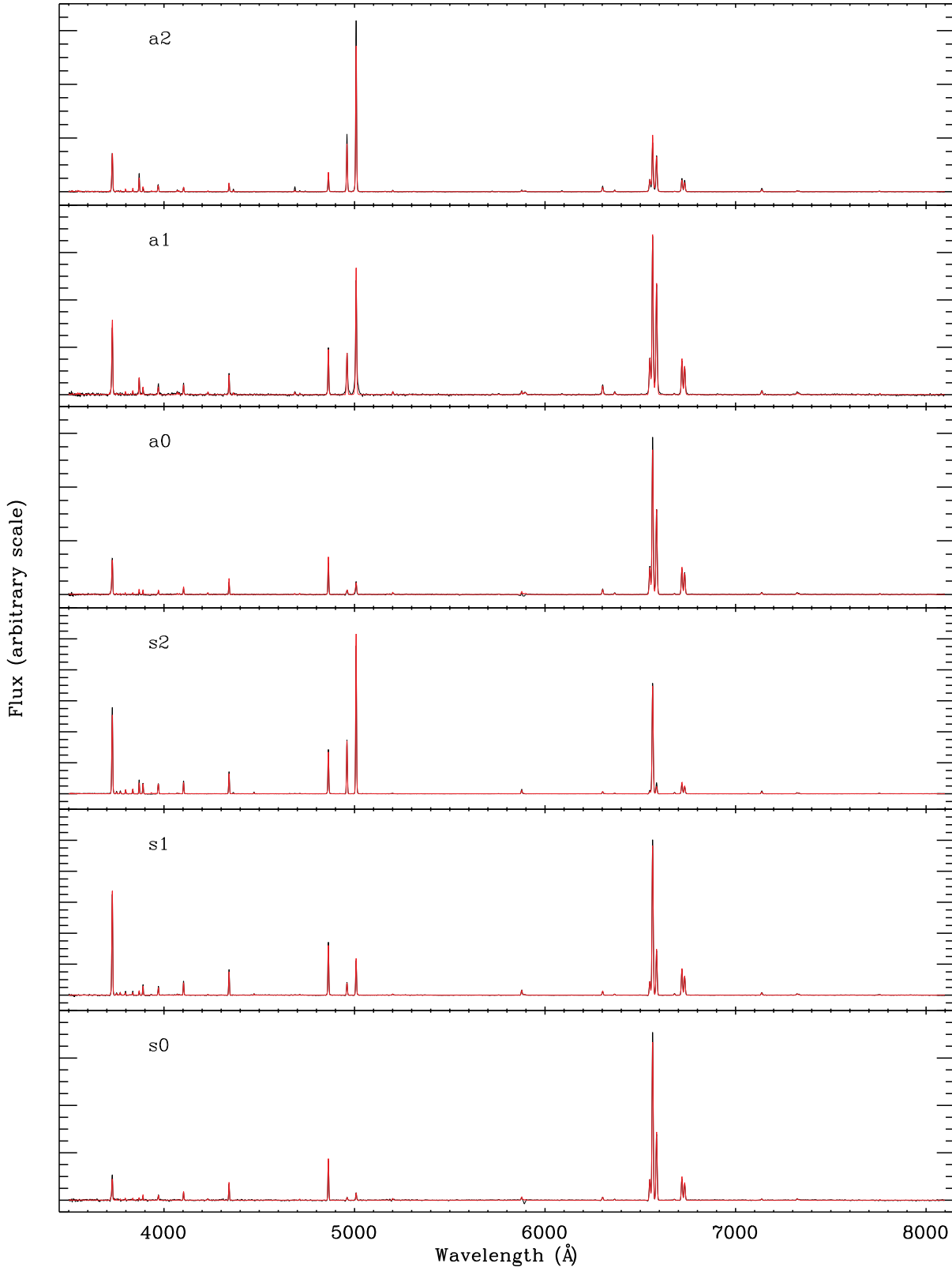


**Figure 20.** Reconstructed MFICA spectra from a range of positions within the AGN (top three panels) and SF (bottom three panels) loci. In each panel the MFICA reconstruction is in red, and a composite of the continuum-subtracted spectra of 50 observed galaxies with similar MFICA weights is in black.

**Table 3.** Measured and dereddened emission line strengths for reconstructed spectra. Measurements are given relative to  $H\beta$ .

Ion	$\lambda_{\text{vac}}$	Measured						Dereddened					
		a0	a1	a2	s0	s1	s2	a0	a1	a2	s0	s1	s2
[O II]	3729	0.98	1.79	2.21	0.53	2.13	1.99	1.80	3.02	3.05	0.97	3.00	2.38
H I	3751	0.01	0.01	0.02	0.02	0.02	0.03	0.03	0.02	0.03	0.03	0.03	0.04
H I	3772	0.00	0.01	0.02	0.01	0.02	0.04	0.01	0.01	0.03	0.01	0.03	0.04
H I	3799	0.02	0.04	0.10	0.02	0.03	0.07	0.03	0.07	0.13	0.04	0.05	0.09
H I	3837	0.03	0.05	0.12	0.03	0.03	0.08	0.05	0.09	0.16	0.05	0.04	0.09
[Ne III]	3870	0.11	0.31	0.55	0.04	0.07	0.18	0.20	0.49	0.74	0.07	0.10	0.22
H I	3890	0.08	0.13	0.23	0.09	0.13	0.21	0.14	0.20	0.31	0.15	0.18	0.24
H I	3971	0.08	0.14	0.25	0.09	0.12	0.20	0.14	0.21	0.33	0.14	0.16	0.23
[S II]	4070	0.02	0.04	0.06	0.01	0.01	0.02	0.03	0.06	0.07	0.02	0.02	0.02
H I	4103	0.17	0.18	0.20	0.17	0.21	0.22	0.26	0.26	0.25	0.27	0.26	0.25
[Fe V]?	4231	0.04	0.04	0.03	0.03	0.02	0.00	0.06	0.06	0.04	0.04	0.02	0.00
H I	4342	0.36	0.37	0.39	0.36	0.41	0.43	0.48	0.47	0.46	0.49	0.48	0.47
[O III]	4364	0.01	0.02	0.04	0.00	0.00	0.01	0.01	0.03	0.05	0.00	0.00	0.01
He I	4473	0.01	0.01	0.01	0.00	0.02	0.02	0.01	0.01	0.01	0.01	0.02	0.02
He II	4687	0.02	0.04	0.05	0.01	0.00	0.00	0.02	0.04	0.05	0.01	0.01	0.00
[Ar IV]	4713	0.02	0.02	0.01	0.02	0.01	0.01	0.02	0.02	0.01	0.02	0.02	0.01
H I	4863	1.00	1.00	1.00	1.00	1.00	1.00	1.00	1.00	1.00	1.00	1.00	1.00
[O III]	4960	0.17	1.04	2.65	0.07	0.25	1.26	0.16	1.00	2.58	0.07	0.25	1.24
[O III]	5008	0.44	3.08	8.02	0.18	0.76	3.90	0.41	2.90	7.72	0.16	0.73	3.81
[N I]	5201	0.06	0.06	0.05	0.05	0.03	0.01	0.05	0.05	0.05	0.04	0.02	0.01
[N II]	5756	0.01	0.01	0.01	0.01	0.01	0.00	0.01	0.01	0.01	0.01	0.00	0.00
He I	5877	0.09	0.08	0.06	0.10	0.12	0.10	0.06	0.06	0.05	0.06	0.09	0.09
Na I	5898	0.05	0.08	0.08	0.02	0.01	0.00	0.03	0.05	0.07	0.01	0.01	0.00
[O I]	6302	0.16	0.25	0.28	0.09	0.10	0.07	0.10	0.16	0.22	0.05	0.08	0.06
[O I]	6366	0.04	0.06	0.08	0.02	0.02	0.02	0.02	0.04	0.06	0.01	0.02	0.02
[N II]	6550	1.07	1.25	1.08	0.75	0.42	0.13	0.61	0.77	0.80	0.43	0.30	0.11
H I	6565	5.06	4.65	3.86	5.01	3.93	3.39	2.86	2.86	2.86	2.86	2.86	2.86
[N II]	6585	3.08	3.45	2.69	2.21	1.23	0.24	1.73	2.11	1.99	1.26	0.89	0.20
He I	6680	0.02	0.02	0.02	0.02	0.03	0.03	0.01	0.01	0.01	0.01	0.02	0.02
[S II]	6718	1.01	1.12	0.86	0.78	0.73	0.38	0.55	0.66	0.62	0.43	0.52	0.32
[S II]	6733	0.78	0.88	0.69	0.58	0.52	0.26	0.42	0.52	0.50	0.32	0.37	0.22
[Ar III]	7138	0.06	0.11	0.15	0.04	0.06	0.07	0.03	0.06	0.10	0.02	0.04	0.06
[O II]	7322	0.06	0.06	0.06	0.05	0.04	0.03	0.03	0.03	0.04	0.02	0.03	0.03
[O II]	7332	0.03	0.04	0.05	0.02	0.03	0.02	0.01	0.02	0.03	0.01	0.02	0.02

lines as faint as 1 per cent of the  $H\beta$  flux, the following investigations rely only on the stronger lines.

### 5.2.2 The AGN locus

We compare the ICA reconstructions to a series of composite models of extended emission regions photoionized by a central continuum source. We follow the Locally Optimally-emitting Cloud (LOC) approach used by Ferguson et al. (1997, hereafter F97) in a similar study, in which the narrow line region (NLR) is modelled as a large number of individual clouds having power law distributions of distance,  $r$ , from a central continuum source and of gas density,  $n$ . Here we present a brief summary of our results to date; the full study will be described in a future paper.

As was done in F97 (see also Baldwin et al. 1995), we model the integrated emitted spectrum of a large number of ionized clouds distributed over a wide range in  $\log(r)$  and  $\log(n)$  with radial distance and density distributions,  $f(r) \propto r^\gamma$  and  $g(n) \propto n^\beta$ , respectively. We use version 10.00 of the plasma simulation code CLOUDY (Ferland et al. 1998) to compute the properties of the individual clouds. Our work builds on the F97 results by optimizing the continuum SED and the chemical abundances in the gas to fit the ICA re-

construction corresponding to a2, the most extreme AGN case.

Fig. 21 shows a subset of diagnostic emission line intensity ratio diagrams calculated for our grids of models, which are shown as filled circles connected by lines. The diagrams also show the points measured from the reconstructed AGN locus, with the point corresponding to the extreme AGN (a2) case shown as the larger filled square. The LOC models shown here use an SED that has been adjusted to improve the fit to the  $I(\text{He I} \lambda 4687)/I(H\beta)$  ratio, which is a well-known SED indicator (Ferland & Osterbrock 1986). An ionizing luminosity,  $L_{\text{ion}} = 10^{43.5} \text{ erg s}^{-1}$ , UV temperature cutoff of  $T_{\text{cut}} = 2.5 \times 10^5 \text{ K}$ , and X-ray to UV ratio of  $\alpha_{\text{ox}} = -1.4$  provide a high-energy edge of the Big Blue Bump that occurs at a somewhat lower energy than in the usual Mathews & Ferland (1987) AGN continuum; the sensitivity of different AGN line ratios to the SED will be discussed in detail in our forthcoming paper. These LOC models use roughly solar abundances (from F97) except that the N/H abundance ratio has been increased to improve the fit to the  $I([\text{N II}] \lambda 6585)/I(\text{H}\alpha)$  ratio. The final abundances relative to hydrogen are: He = -0.987, Li = -8.69, Be = -10.58, B = -9.12, C = -3.61, N = -3.73, O = -3.31, F = -7.52, Ne = -3.92, Na = -5.68, Mg = -4.42,

Al = -5.51, Si = -4.49, P = -6.43, S = -4.80, Cl = -6.72, Ar = -5.60, K = -6.87, Ca = -5.65, Sc = -8.80, Ti = -6.96, V = -7.98, Cr = -6.32, Fe = -4.54, Co = -7.08, Ni = -5.75, Cu = -7.73, Zn = -7.34.

The fits to the a2 point are not perfect, but for  $\beta = -1.4$  and  $\gamma = -0.75$  are correct to within a factor of two. The fits to the points further down the AGN locus remain unclear, although for a1 values of  $\beta = -1.4$  and  $\gamma = -0.25$  appear to give the best fit. The a0 reconstruction does not fit neatly on these sequences and is likely to represent a composite of more than one source of excitation. The manner in which the loci were constructed limits the potential contribution from star formation, but contributions due to shock-heated gas or excitation due to LINERs remain possibilities. In contrast, the reconstructed MFICA spectra along the upper part of the AGN sequence can be understood physically in terms of a rather simple NLR model with photoionization by a single central engine.

### 5.2.3 The star formation locus

Table 3 and Fig. 20 show that the  $\text{He I} \lambda 5877/\text{H}\beta$  ratio is in the range 0.09 for the s2 and s1 reconstructions to 0.06 for the s0 reconstruction. Here we show that this ratio can be used to estimate the starburst age.

In H II regions optical He I and  $\text{H}\beta$  lines form by recombination from  $\text{He}^+$  and  $\text{H}^+$ . The  $\text{He I}/\text{H}\beta$  intensity ratio is proportional to the ratio of abundances of these ions. The small  $\text{He I}/\text{H}\beta$  ratios found here are unlikely to reflect a truly low He/H abundance ratio. The lower bound to the range of He/H that can occur in a galaxy is that produced by Big Bang nucleosynthesis (Osterbrock & Ferland 2006, Chapter 9),  $\text{He}/\text{H} \sim 0.08$ . If both He and H are singly ionized this abundance ratio corresponds to  $I(\text{He I} \lambda 5877)/I(\text{H}\beta) \sim 0.12$ , where the recombination coefficients listed in Osterbrock & Ferland (2006) are adopted, and pure recombination is assumed. There will be a collisional contribution which will increase the ratio for some of the denser models considered below.

The observed intensity ratio is smaller than this lower limit, suggesting that the  $\text{He}^+/\text{H}^+$  ratio is smaller than the He/H abundance ratio. Helium has two ionized states,  $\text{He}^+$  and  $\text{He}^{++}$ , and high-ionization nebulae can have significant amounts of  $\text{He}^{++}$ , which produces He II emission. However the lack of  $\text{He II} \lambda 4687$  emission shows that this is not important in our sample and is consistent with the emission coming from H II regions rather than AGN or evolved objects like planetary nebulae. This means that helium must be present in either atomic or singly ionized form in regions where hydrogen is ionized.

It is most likely that there are significant parts of the H II regions where hydrogen is ionized but He is atomic and produces no recombination emission. This happens in H II regions ionized by relatively cool stars because of the higher ionization potential of helium. In this case the  $\text{He I}/\text{H I}$  intensity ratio is mainly set by the SED, as we show next.

Fig. 22 quantifies the effect of the SED on the  $\text{He I}/\text{H I}$  intensity ratio. In photoionization equilibrium the ionization of the gas is determined both by the SED and by the ionization parameter,  $U$ , the dimensionless ratio of ionizing photon to hydrogen densities. The  $x$ -axis corresponds to varying SED shapes, given as the stellar effective temperature as

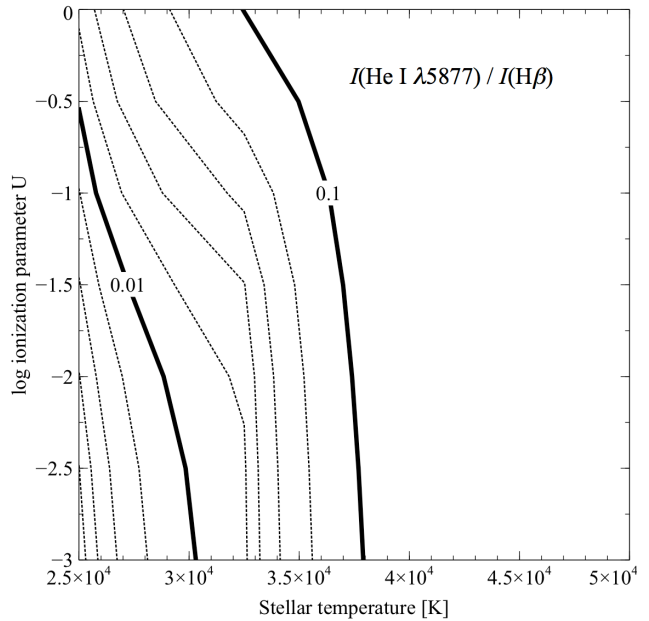


**Figure 22.** Intensity ratio  $I(\text{He I} \lambda 5877)/I(\text{H}\beta)$  for gas photoionized by stellar SEDs, for a range of ionization parameters and stellar effective temperatures.

suming the TLUSTY grids of atmospheres (Lanz & Hubeny 2003, 2007). The  $y$ -axis gives the log of the ionization parameter, the second parameter that sets the ionization of the gas. The contours show the  $\text{He I} \lambda 5877/\text{H}\beta$  ratio computed with CLOUDY. Galactic ISM abundances and dust were assumed along with a hydrogen density of  $10^3 \text{ cm}^{-3}$ , typical of H II regions. The geometry was assumed to be a plane parallel layer, a good approximation to blister H II regions in 30 Dor (Pellegrini, Baldwin & Ferland 2010).

There are two regimes seen in Fig. 22. For stellar temperatures higher than 38 000 K, corresponding to the O stars that dominate the SED of the youngest star clusters, the intensity ratio  $I(\text{He I} \lambda 5877)/I(\text{H}\beta) \geq 0.12$  is nearly constant, set by the He/H ratio in the host galaxy. This regime fills the right hand half of Fig. 22. For lower effective temperatures, and hence older clusters, the situation becomes more complex; in this regime the  $\text{He I}/\text{H}\beta$  ratio shows dependencies on both the stellar temperature and the ionization parameter.

As the cluster ages and the SED grows softer it moves to the left in Fig. 22. The  $\text{He I}/\text{H}\beta$  ratio will be constant until the cluster reaches an age such that stars with  $T_{\text{eff}} \geq 38 000 \text{ K}$  die, at which point the  $\text{He I}/\text{H}\beta$  ratio will begin to decrease. The hot-star calibration given by Heap, Lanz & Hubeny (2006), which is also based on the TLUSTY stellar atmospheres used to make Fig. 22, shows that 38 000 K corresponds to an O6.5 V star with a mass of  $29 \text{ M}_\odot$  and a main-sequence lifetime of 6 Myr (Schaller et al. 1992).

We further quantify the transition between the two regimes by computing the SED produced by an evolving star cluster using a series of Starburst99 (Leitherer et al. 1999; Vázquez & Leitherer 2005) models. Instantaneous formation was assumed, using a Kroupa (2001) IMF truncated at 0.1 and  $100 \text{ M}_\odot$ , and solar metallicity. This fully specifies the SED as a function of time. In terms of fundamental parameters, the ionization parameter – which depends on the cluster

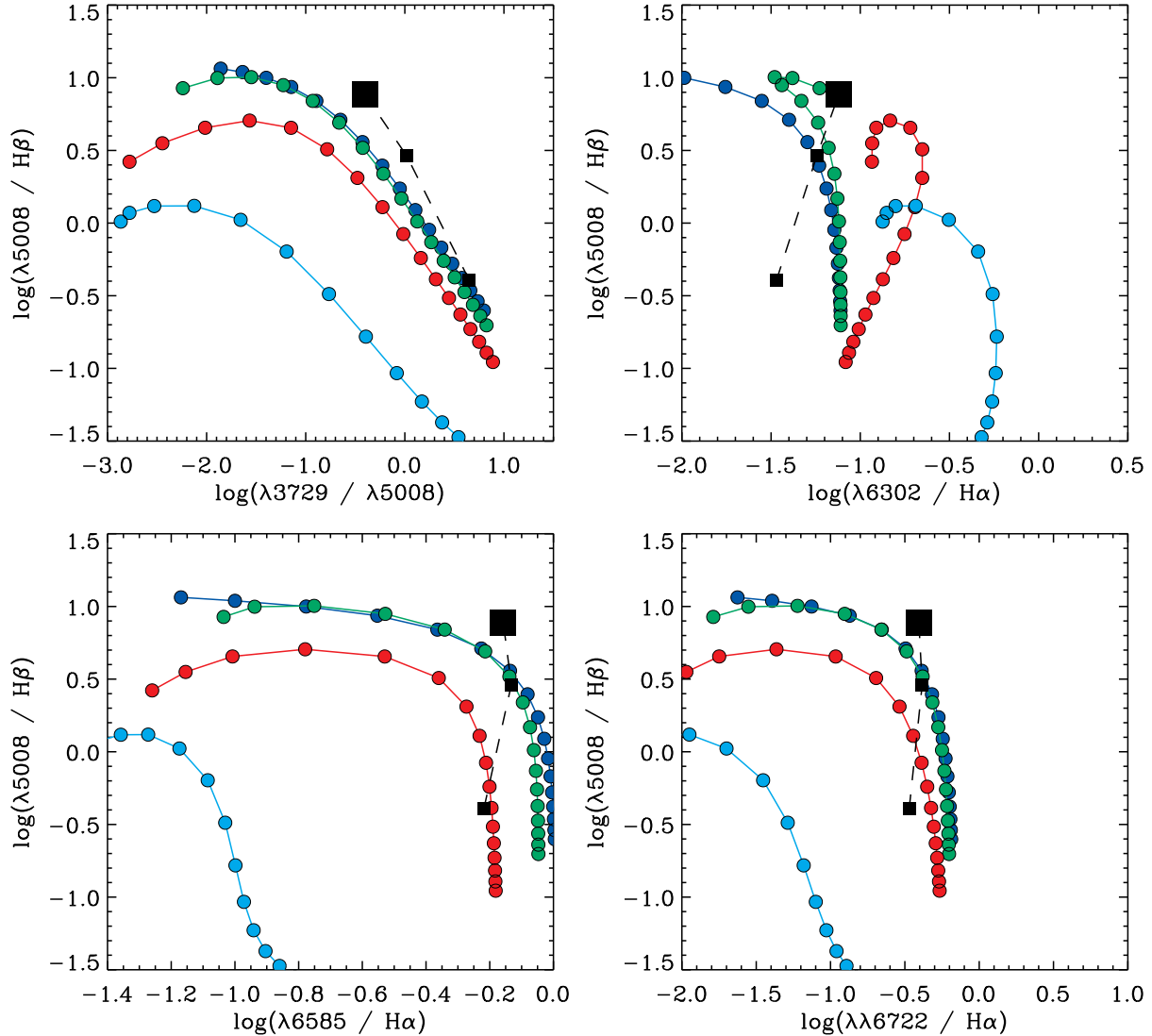


**Figure 21.** A subset of line-ratio diagrams are given here in the spirit of F97. In each panel the filled squares connected by the dashed line are the dereddened measurements from the a2-a1-a0 sequence of reconstructed spectra, with the large square representing the a2 point. The free parameters are displayed for  $\beta = -0.6$  (aqua),  $-1.0$  (red),  $-1.4$  (green),  $-1.8$  (blue) and for  $-2.0 \leq \gamma \leq 2.0$  in increments of  $0.25$  where the most negative  $\gamma$  values correspond to the highest values along the  $y$ -axis. The a2 points are successfully fitted by  $(\beta = -1.4, \gamma = -0.75)$ , and the a1 points by  $(\beta = -1.4, \gamma = -0.25)$ , but the physical properties of the a0 reconstruction remain unclear.

luminosity, the separation between the cluster and the gas, and the gas density – is the remaining unknown. A real environment is likely to be highly chaotic, much like the Magellanic Clouds, with shock-heated hot gas intermixed with molecular clouds (Pellegrini et al. 2010; Pellegrini, Baldwin & Ferland 2011). Such an environment would not have a single ionization parameter, but rather would be a mix of clouds with a wide range (Pellegrini et al. 2011), as is described by LOC models.

Fig. 23 shows contour plots of the  $\text{He I} \lambda 5877$  and  $\text{H}\beta$  equivalent widths for starburst models all having the same ionizing luminosity but with ages between 1 and 8 Myr. The horizontal axis is the hydrogen density  $n_{\text{H}}$ , while the vertical axis is the distance  $R$  from the ionizing continuum source. Note the wide range of densities in the figure. The  $\text{He I}$  lines

will be enhanced by a collisional contribution for such conditions (Ferland 1986). Lines of constant ionization parameter  $U \propto R^{-2} n_{\text{H}}^{-1}$  would run diagonally across these plots, so the starburst age, ionization parameter space discussed above is represented on Fig. 23. It is seen that while  $\text{H}\beta$  comes from most of the  $n_{\text{H}}$ ,  $R$  plane for all ages, the  $\text{He I} \lambda 5877$  emission comes from only a restricted area by the time an age of 6 Myr is reached, and then is entirely absent by 8 Myr.

Fig. 24 shows a series of plots of the  $\text{He I}/\text{H}\beta$  intensity ratio vs. age, made for the locations on the  $n_{\text{H}}$ ,  $R$  plane marked by the open circles in the bottom-left panel of Fig. 23. The heavy red line on Fig. 24 is the average, corresponding to a LOC model with equal numbers of clouds as a function of  $\log(n_{\text{H}})$  and  $\log(R)$ . The  $\text{He I}/\text{H}\beta$  ratio integrated over the full  $n_{\text{H}}$ ,  $R$  plane will drop off sharply, as

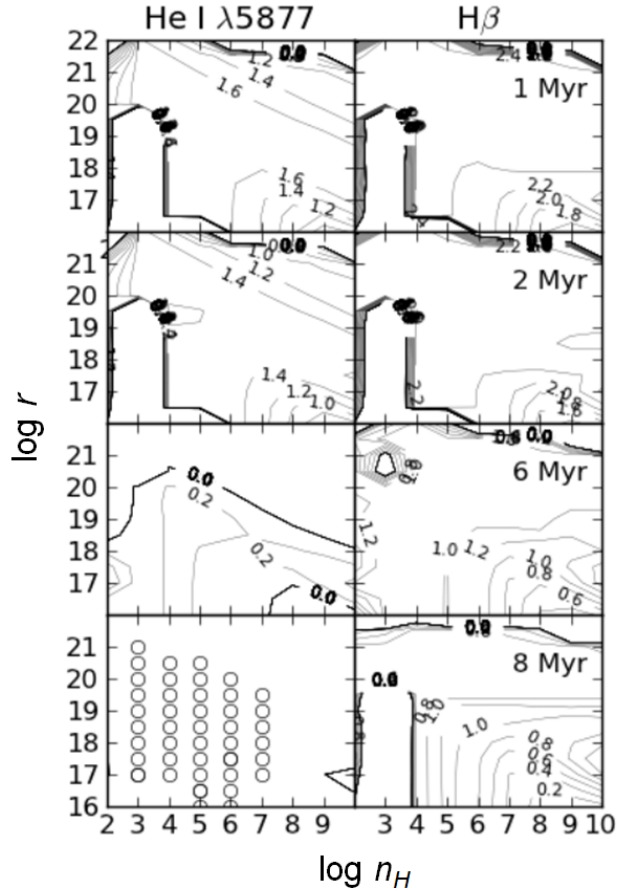


**Figure 23.** Contour plots showing the equivalent widths of  $\text{He I} \lambda 5877$  and  $\text{H}\beta$  lines emitted by gas clouds as a function of their hydrogen density  $n_H$  and their distance  $R$  from starbursts of equal ionizing luminosity. The starbursts have different ages, as indicated in the right-hand panel in each row. The circles in the bottom-left panel show the  $n_H, R$  values of the curves plotted in Fig. 24.

discussed above, with the exact cutoff age depending on the distribution of the emitting clouds in  $n_H$  and  $R$ . The values  $\text{He I}/\text{H}\beta = 0.06-0.09$  measured for MFICA reconstructions are consistent with a single starburst with an age of about 7 Myr. But they might also be due to a mix of star-forming regions within each individual galaxy, with half of the  $\text{H}\beta$  emission coming from gas ionized by stars sufficiently younger than 7 Myr that their  $\text{He I}/\text{H}\beta$  ratio is at the maximum value, and the other half coming from regions ionized by older stars with no  $\text{He}^+$  being formed. In a future paper we will test this hypothesis by comparing detailed LOC models to the intensity ratios of the wide variety of weak emission lines that can be measured using the MFICA technique.

## 6 CONCLUSIONS

In this paper we have presented an analysis of narrow emission-line galaxies based on the MFICA technique. A set of five continuum components was generated from a mixed sample of galaxies with and without emission lines. Three of

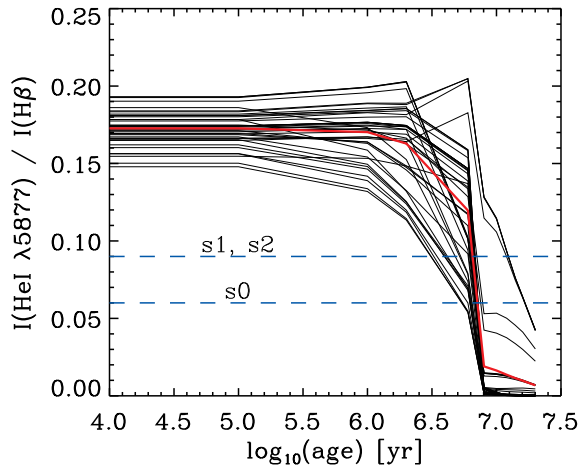


**Figure 24.** The  $\text{He I}/\text{H}\beta$  intensity ratio as a function of starburst age. The thin black lines are for each of the  $n_H, R$  points marked by the circles on the bottom-left panel in Fig. 23. The heavy red line is the average of all the thin lines. The horizontal dashed lines show the measured  $\text{He I}/\text{H}\beta$  ratios for ICA reconstructions  $s_0, s_1$  and  $s_2$ .

these components can be identified with old, intermediate and young stellar populations, while the final two components allow the reconstruction of the full range of ages of stellar populations. Using these components to fit and subtract the continuum from a sample of emission-line galaxies, we then generated a set of five emission-line components. In combination, the five continuum and five emission-line components can be used to produce accurate reconstructions of the spectra of galaxies with a wide range of properties.

We have provided a brief demonstration of the strong correlations between the MFICA continuum weights and the VESPA star formation histories presented by Tojeiro et al. (2009). These correlations imply that it will be possible to derive estimated star formation histories for individual galaxies based on the MFICA results.

After identifying the regions of parameter space that correspond to pure star formation and pure AGN, we made use of the high S/N MFICA reconstructions to probe the physical conditions within these systems. The most extreme AGN case is well fit by a model consisting of a large number of ionized clouds with radial distance and density distributions,  $f(r) \propto r^\gamma$  and  $g(n) \propto n^\beta$ , respectively, with  $\gamma = -0.75$  and  $\beta = -1.4$ . In the star formation reconstructions, the measured  $\text{He I} \lambda 5877/\text{H}\beta$  ratios imply a starburst age of about 7 Myr, or a mix of star-forming regions both older and younger than 7 Myr.

A full analysis of the reconstructed spectra is deferred to a forthcoming paper, but the initial investigations presented here serve to illustrate the power of MFICA to probe the physical conditions present within large samples of galaxies. Techniques of this sort will prove invaluable in the analysis of current and future large-scale spectroscopic surveys.

## ACKNOWLEDGMENTS

We are grateful to Manda Banerji for helpful discussions. We thank the anonymous referee for a thoughtful and in-depth review. JTA acknowledges the award of an STFC Ph.D. studentship and an ARC Super Science Fellowship. PCH acknowledges support from the STFC-funded Galaxy Formation and Evolution programme at the Institute of Astronomy. JAB and CTR acknowledge support from NASA ADP grant NNX10AD05G and NSF grant AST-1006593. GJF acknowledges support by NSF (0908877, 1108928 and 1109061), NASA (07-ATFP07-0124, 10-ATP10-0053 and 10-ADAP10-0073), JPL (RSA No 1430426), and STScI (HST-AR-12125.01 and HST-GO-12309). We wish to acknowledge the support of the Michigan State University High Performance Computing Center and the Institute for Cyber Enabled Research.

The Max Plank institute for Astrophysics/John Hopkins University (MPA/JHU) SDSS data base was produced by a collaboration of researchers (currently or formerly) from the MPA and the JHU. The team is made up of Stephane Charlot (IAP), Guinevere Kauffmann and Simon White (MPA), Tim Heckman (JHU), Christy Tremonti (U. Wisconsin-Madison – formerly JHU) and Jarle Brinchmann (Leiden University – formerly MPA).

Funding for the SDSS and SDSS-II has been provided by the Alfred P. Sloan Foundation, the Participating Institutions, the National Science Foundation, the U.S. Department of Energy, the National Aeronautics and Space Administration, the Japanese Monbukagakusho, the Max Planck Society, and the Higher Education Funding Council for England. The SDSS Web Site is <http://www.sdss.org/>.

The SDSS is managed by the Astrophysical Research Consortium for the Participating Institutions. The Participating Institutions are the American Museum of Natural History, Astrophysical Institute Potsdam, University of Basel, University of Cambridge, Case Western Reserve University, University of Chicago, Drexel University, Fermilab, the Institute for Advanced Study, the Japan Participation Group, Johns Hopkins University, the Joint Institute for Nuclear Astrophysics, the Kavli Institute for Particle Astrophysics and Cosmology, the Korean Scientist Group, the Chinese Academy of Sciences (LAMOST), Los Alamos National Laboratory, the Max-Planck-Institute for Astronomy (MPIA), the Max-Planck-Institute for Astrophysics (MPA), New Mexico State University, Ohio State University, University of Pittsburgh, University of Portsmouth, Princeton University, the United States Naval Observatory, and the University of Washington.

## REFERENCES

Abazajian K. N., et al., 2009, *ApJS*, 182, 543  
 Allen J. T., Hewett P. C., Maddox N., Richards G. T., Belokurov V., 2011, *MNRAS*, 410, 860  
 Baldwin J., Ferland G., Korista K., Verner D., 1995, *ApJ*, 455, L119+  
 Baldwin J. A., Phillips M. M., Terlevich R., 1981, *PASP*, 93, 5  
 Blanton M. R., Roweis S., 2007, *AJ*, 133, 734  
 Bruzual G., Charlot S., 2003, *MNRAS*, 344, 1000  
 Cardelli J. A., Clayton G. C., Mathis J. S., 1989, *ApJ*, 345, 245  
 Charlot S., Fall S. M., 2000, *ApJ*, 539, 718  
 Croton D. J., et al., 2006, *MNRAS*, 365, 11  
 Diaz A. I., Pagel B. E. J., Wilson I. R. G., 1985, *MNRAS*, 212, 737  
 Draine B. T., 2011, Physics of the Interstellar and Inter-galactic Medium  
 Ferguson J. W., Korista K. T., Baldwin J. A., Ferland G. J., 1997, *ApJ*, 487, 122  
 Ferland G. J., 1986, *ApJ*, 310, L67  
 Ferland G. J., Korista K. T., Verner D. A., Ferguson J. W., Kingdon J. B., Verner E. M., 1998, *PASP*, 110, 761  
 Ferland G. J., Osterbrock D. E., 1986, *ApJ*, 300, 658  
 Ferrarese L., Merritt D., 2000, *ApJ*, 539, L9  
 Francis P. J., Hewett P. C., Foltz C. B., Chaffee F. H., 1992, *ApJ*, 398, 476  
 Granato G. L., De Zotti G., Silva L., Bressan A., Danese L., 2004, *ApJ*, 600, 580  
 Häring N., Rix H., 2004, *ApJ*, 604, L89  
 Heap S. R., Lanz T., Hubeny I., 2006, *ApJ*, 638, 409  
 Højen-Sørensen P. A., Winther O., Hansen L. K., 2002, *Neural Computation*, 14, 889  
 Juneau S., Dickinson M., Alexander D. M., Salim S., 2011, *ApJ*, 736, 104  
 Kauffmann G., et al., 2003, *MNRAS*, 346, 1055  
 Kewley L. J., Dopita M. A., Sutherland R. S., Heisler C. A., Trevena J., 2001, *ApJ*, 556, 121  
 Kewley L. J., Groves B., Kauffmann G., Heckman T., 2006, *MNRAS*, 372, 961  
 Kormendy J., Gebhardt K., 2001, in J. C. Wheeler & H. Martel ed., 20th Texas Symposium on relativistic astrophysics Vol. 586 of American Institute of Physics Conference Series, Supermassive black holes in galactic nuclei. pp 363–381  
 Kroupa P., 2001, *MNRAS*, 322, 231  
 Lamareille F., 2010, *A&A*, 509, A53+  
 Lamareille F., Mouhcine M., Contini T., Lewis I., Maddox S., 2004, *MNRAS*, 350, 396  
 Lanz T., Hubeny I., 2003, *ApJS*, 146, 417  
 Lanz T., Hubeny I., 2007, *ApJS*, 169, 83  
 Leitherer C., et al., 1999, *ApJS*, 123, 3  
 Lu H., Zhou H., Wang J., Wang T., Dong X., Zhuang Z., Li C., 2006, *AJ*, 131, 790  
 Magorrian J., et al., 1998, *AJ*, 115, 2285  
 Marocco J., Hache E., Lamareille F., 2011, *A&A*, 531, A71+  
 Mathews W. G., Ferland G. J., 1987, *ApJ*, 323, 456  
 Mittaz J. P. D., Penston M. V., Snijders M. A. J., 1990, *MNRAS*, 242, 370  
 Newberg H. J., Yanny B., 1997, *ApJS*, 113, 89  
 Opper M., Winther O., 2005, *Journal of Machine Learning Research*, 6, 2177  
 Osterbrock D. E., Ferland G. J., 2006, *Astrophysics of gaseous nebulae and active galactic nuclei*. California: University Science Books  
 Osterbrock D. E., Tran H. D., Veilleux S., 1992, *ApJ*, 389, 196  
 Pellegrini E. W., Baldwin J. A., Ferland G. J., 2010, *ApJS*, 191, 160  
 Pellegrini E. W., Baldwin J. A., Ferland G. J., 2011, *ApJ*, 738, 34

Sarzi M., et al., 2006, MNRAS, 366, 1151  
 Schaller G., Schaefer D., Meynet G., Maeder A., 1992,  
 A&AS, 96, 269  
 Schawinski K., et al., 2007, MNRAS, 382, 1415  
 Schlegel D. J., Finkbeiner D. P., Davis M., 1998, ApJ, 500,  
 525  
 Springel V., Di Matteo T., Hernquist L., 2005, MNRAS,  
 361, 776  
 Stasińska G., Cid Fernandes R., Mateus A., Sodré L., Asari  
 N. V., 2006, MNRAS, 371, 972  
 Tojeiro R., Heavens A. F., Jimenez R., Panter B., 2007,  
 MNRAS, 381, 1252  
 Tojeiro R., Wilkins S., Heavens A. F., Panter B., Jimenez  
 R., 2009, ApJS, 185, 1  
 Vázquez G. A., Leitherer C., 2005, ApJ, 621, 695  
 Veilleux S., Osterbrock D. E., 1987, ApJS, 63, 295  
 Wild V., Heckman T., Charlot S., 2010, MNRAS, 405, 933  
 Wild V., Hewett P. C., 2005, MNRAS, 358, 1083  
 Worthey G., Faber S. M., Gonzalez J. J., Burstein D., 1994,  
 ApJS, 94, 687  
 Yan R., et al., 2011, ApJ, 728, 38  
 Yip C., et al., 2004, AJ, 128, 585  
 York D. G., et al., 2000, AJ, 120, 1579